**TECHNISCHE
UNIVERSITÄT
WIEN**
Vienna University of Technology

DIPLOMARBEIT

SYNTHESIS OF GERMANIUM NANOSTRUCTURES BY A MICROWAVE APPROACH

AUSGEFÜHRT AM INSTITUT FÜR MATERIALCHEMIE
DER TECHNISCHEN UNIVERSITÄT WIEN

UNTER ANLEITUNG VON

DR. RER. NAT. SVEN CHRISTIAN BARTH

O. UNIV. PROF. DR. RER. NAT. ULRICH SCHUBERT

DURCH

YULIA POPOVA, BSc.

MÄRZSTRAße 73/6
1150 WIEN

WIEN, JANUAR 2015

We can't solve problems by using the same kind of thinking we used when we created them.

--Albert Einstein, (1879-1955)

EIDESSTATTLICHE ERKLÄRUNG

Ich erkläre hiermit an Eides statt, dass ich die vorliegende Diplomarbeit selbstständig und ohne fremde Hilfe verfasst, andere als angegebenen Quellen und Hilfsmittel nicht benutzt und die den benutzten Quellen wörtlich und inhaltlich entnommenen Stellen als solche erkenntlich gemacht habe.

STATUTORY DECLARATION

I herewith declare that I have authored this thesis independently, that I have not used other than the declared sources / resources, and that I have explicitly marked all material which has been quoted either literally or by content from used sources.

ACKNOWLEDGEMENT

I want to thank…

… my supervisor Dr. Sven Barth for giving me an opportunity to work on an interesting and up to date project, for helping me to fill the basic knowledge gap, for being patient, helpful and encouraging, for stimulating and motivating me to work and learn independently and to find solutions for current issues myself.

… Prof. Dr. U. Schubert for being my thesis' supervisor and for giving me the chance to work within his research group.

… my family and especially my mother without whom my studies would never have been possible. For her financial support throughout my studies, for the enormous encouragement and comprehension, for respecting my choice to study abroad and supporting me in all my decisions. I will never forget the huge contribution in helping me finish this work.

… my colleagues from the Institute of Material Chemistry for the nice working atmosphere, for the empathy with my problems and non-working reactions and for being available to help anytime.

… Patrik P. for being a great lab colleague, for encouraging me, for being helpful at any time and for XRD measurements.

… Felix B. for creating a cheerful and amusing atmosphere, for sharing his experience and knowledge, for being helpful at any time, for XRD and NMR measurements.

… Matthias Cz. for sharing his knowledge and experience about DLS.

ABSTRACT

In this thesis the synthesis of germanium nanostructures via thermal decomposition in a microwave reactor is presented. The investigation includes the synthesis of elongated germanium nanostructures varying decomposition temperature, reaction time and precursor concentration of the precursors. Tin nanoparticles have been used as catalyst seeds for metal-assisted growth of germanium nanostructures, which have been characterized via DLS spectroscopy, powder X-ray diffraction, SEM and TEM.

This work is divided into two main parts. The first part describes the attempt to synthesize crystalline germanium elongated nanostructures. The second part is dedicated to the synthesis of tin nanoparticles with narrow size distribution and diameters under 10 nm that can be later used as metallic catalyst seeds for germanium nanostructures synthesis.

The resulting materials are slightly elongated (aspect ratio ca. 1 : 5) crystalline germanium nanostructures with a relatively broad size distribution and containing tin nanoparticles in their structure. The tin nanoparticles obtained by one of the synthetic routes described below have a narrow size distribution of about 2 % and their size in different experiments varies in 5 – 15 nm range.

KURZFASSUNG

In dieser Arbeit wird die Synthese und Charakterisierung von Germanium-Nanostrukturen, die mittels thermischer Zersetzung in einem Mikrowellenreaktor hergestellt wurden, beschrieben. Die Untersuchung enthält die Synthese der moderat elongierten Germanium-Nanostrukturen unter Variation der Reaktionstemperatur, Reaktionszeit und Konzentration des Precursors. Zinn-Nanopartikel wurden als Katalysatorkeime für das metallunterstützte Wachstum von Germanium-Nanostrukturen verwendet. Die hergestellten Nanostrukturen wurden durch DLS Spektroskopie, Pulverdiffraktometrie und Elektronenmikroskopie (SEM bzw. TEM) charakterisiert.

Diese Arbeit besteht aus zwei Teilen. Der erste Teil beschäftigt sich mit dem Versuch kristalline gleichförmige Germanium-Nanostrukturen mit geringer Größenverteilung herzustellen. Der zweite Teil beschreibt die Synthese der Zinn-Nanopartikel mit geringer Größenverteilung, die danach als Katalysatorkeime für die Germanium-Nanostruktursynthese angewandt werden können.

Die hergestellte Materialen sind moderat elongierte (Länge-zu-Dickenverhältnis ca. 1 : 5) kristalline Germanium-Nanostrukturen mit Sn-Nanopartikeln mit breiter Größenverteilung. Die hergestellten Zinn-Nanopartikel weisen eine ziemlich geringe Größenverteilung ca. 2 % auf und befinden sich im 5 – 15 nm Größenbereich (je nach dem Versuch).

TABLE OF CONTENTS

1. INTRODUCTION

The development of new materials and new methods of their production has become crucial in the modern world. Every material has its unique set of physical, chemical, electric, thermal, optical and other properties that would be suitable for certain applications. The development of new materials is intended to solve this particular problem. New synthetic routes and further functionalization are meant to enhance the properties of certain materials. Despite many already known and commonly used synthetic routes, one always tries to find more cost effective, and more time and energy efficient methods. The search for new and cheaper precursors that do not produce unwanted by-products as they decompose, give higher yield, and higher purity materials with better characteristics, is also an important part of the expansion of the new synthetic techniques. Microwave-assisted growth of germanium nanostructures is a new promising method of obtaining monodisperse crystalline germanium nanoparticles and nanorods.[1-3]

1.1. NANOSTRUCTURED MATERIALS SYNTHESIS

Nowadays various synthetic methods are known in nanomaterials synthesis. There are two main paradigms for synthesis of nanomaterials. Top-down techniques, such as chemical etching and mechanical attrition which are among the most common methodologies, are based on the reduction of larger entities into nanoscale objects.[4,5] During the process of the attrition, powder particles undergo a mechanical deformation through the extending along shear bands causing dislocations. Over time fine-grained nanostructures are obtained. The size of the nanoparticles obtained with this technique can reach between 2 to 20 nm. Chemical etching is often used to obtain 1D nanostructures (such structures have two dimensions in the nanoscale, but the length could be much greater), as it is eligible for many

materials especially for semiconductors. After the mask material has been applied on top of the sample, the etching solution is added and it removes material from the uncovered areas. Such techniques also allow the synthesis of structures less than 20 nm in size.[6]

Bottom-up techniques are performed either in a gas phase or in a solution. It includes such methods as controlled precipitation or crystallization from a solution, sol-gel processing, reactions in confined spaces, condensation from the gas phase, chemical vapour transport, aerosol processes *etc.* The chemical vapour transport principle can be described as an exothermic or endothermic reaction between precursors in solid state and in gas phase. The driving force in this case is the temperature gradient that provides the mass transport of a product via gas phase from one site to another. Aerosol synthesis is based on the gas phase reactions with the formation of the product in a solid state, usually small particles. A precipitation or crystallization method has as its general principle the formation of particles from a sufficiently concentrated solution. As far as sol-gel processing is concerned the solid products are obtained by gelation. The first step of this process is the formation of a colloidal solution (sol) by a hydrolysis or a polycondensation reaction, which is then transformed into a gel, an agglomeration of colloidal particles that are surrounded and support the liquid phase. [6]

The metal-assisted growth is one of the most commonly used techniques for 1D nanostructure synthesis because of its potential to control and change the conditions in order to obtain different structures and morphologies. The VLS (vapour-liquid-solid) single crystal growth mechanism from a vapour phase was first described by Wagner and Ellis.[7] Metal-assisted growth in liquids is similar to that in a vapour phase. As the solution is heated and the precursors start to decompose, two elements form a liquid alloy droplet according to their phase diagram. The decomposition occurs preferentially on the droplet interface. The droplet eventually becomes supersaturated and an inorganic crystal starts to nucleate on the solid-liquid interface. This mechanism depends on two processes: absorption of structure forming species from the solution where the precursor is dissolved, and precipitation of the source materials at the particle-substrate interface. If the process

takes place in a solution the mechanism is called solution-liquid-solid (SLS). In the case of vapour-liquid-solid (VLS) mechanism the growth process proceeds via the gas phase. There are some cases when the growing material is able to dissolve in the solid catalyst seed and the corresponding mechanism is called solution-solid-solid (SSS).[8]

1.2. GERMANIUM NANOCRYSTALS SYNTHESIS

Several synthetic methods have been investigated over the past few decades. One can distinguish between the solution and the gas phase synthetic methods. There are two groups of methods depending on the reaction type that can be performed in the solution as well as in the gas phase, i.e. thermal decomposition of organogermane precursors and thermal reduction of organic and inorganic germanium compounds. The reduction of germanium tetrachloride, metathesis reaction of germanium Zintl salts, thermal decomposition of organogermane precursors in high-boiling solvents, thermal reduction of organogermanium precursors, one-pot heat-up methods and the reduction of inorganic germanium salts with hydrides or butyllithium are among the most common synthesis routes in solution.[9]

Chiu *et al.* have described a method where $GeCl_4$ has been reduced with sodium naphtalide at room temperature using Schlenk technique. After the following addition of n-butylmagnesium chloride and removing of the organic side products crystalline germanium nanoparticles of about 4 nm in diameter were obtained.[10] Zintl salts such as sodium germanide (NaGe), potassium germanide (KGe) or magnesium germanide (Mg_2Ge) perform a metathesis reaction with germanium inorganic salts such as $GeCl_4$ resulting in 1 to 5 nm crystalline alkyl-terminated germanium nanoparticles with narrow size distribution after refluxing for several hours in diethylene glycol dibutyl ether.[11] Similar synthetic routes were also described by Taylor *et al.* and by Tanke *et al.*[12,13] There are several papers that

describe the formation of germanium nanocrystals by sol-gel process where the organogermanium precursors, such as tetraethoxyorthogermanate (Ge(OEt)$_4$) or organotrichlorogermanes (C$_3$H$_5$GeCl$_3$, C$_7$H$_7$GeCl$_3$, t-C$_4$H$_9$GeCl$_3$, n-C$_4$H$_9$GeCl$_3$, HOOCC$_2$H$_4$GeCl$_3$) undergo hydrolysis and condensation processes that result in germanium nanostructures embedded either in silica[14,15] or germanium (IV) oxide[16] matrix. One of the most common approaches in solution synthesis remains as the reduction of inorganic germanium salts such as GeCl$_4$, GeI$_4$, GeI$_2$ using inorganic hydrides or butyllithium as strong reducing agents. Thus, Wu *et al.*[17] described the reduction of germanium tetrachloride at room temperature using an ultrasonic bath and sodium borohydride, lithium aluminium hydride and hydrazine (N$_2$H$_4$·H$_2$O) as reducing agents. The obtained germanium nanoparticles were crystalline from 4 to 7 nm in diameter depending on the reducing agent with relatively narrow size distribution. The reduction reaction can be performed at room temperature using stronger reducing agents[18,19] as well as using the conventional heating. Lu *et al.* reported the synthesis of colloidal germanium nanocrystals at 300 ^{o}C using a highly reactive germanium (II) iodide, which is reduced by lithium aluminium hydride to germanium with formation of germanium (IV) iodide as a by-product. The reaction is performed in tri-*n*-octylphosphine (TOP) used as a coordinating solvent. Crystalline germanium nanoparticles from 3 to 12 nm in diameter were obtained depending on the concentration of the precursor.[20] As far as the reduction with n-butyllithium as a reducing agent is concerned, Lee *et al.* reported a hot injection method at 300 ^{o}C using GeI$_2$ as a precursor in order to obtain 4 nm germanium nanocrystals.[21] Germanium iodide (GeI$_2$) is a highly reactive precursor, but due to its high cost it is not as commonly used as, for instance, GeCl$_4$.

Thermal decomposition of organogermane precursors such as tetraethylgermane or germanium (II) bis[bis(trimethylsilyl)amide] require high temperatures for germanium in order to crystalize. Hence, it is necessary to use organic solvents with a high boiling point. Thus, Zaitseva *et al.* reported the synthesis of colloidal germanium nanoparticles by hot injection method using tri-*n*-octylamine (TOA, C$_{24}$H$_{51}$N, b.p. 366 ^{o}C), squalene (C$_{30}$H$_{50}$, b.p.

285 °C), and octacosane ($C_{28}H_{58}$, b.p. 278 °C) as solvents.[22] The obtained nanoparticles were crystalline and from 4 to 11 nm in diameter depending on the solvent and the organogermane precursor (Trichlorogermane (TCG), Tetraethylgermane (TEG), Tetrabutylgermane (TBG)) used. Schrick *et al.* took oligogermane ($Bu^n_3GeGePh_2GeBu^n_3$) as a precursor and described the method of hot injection using a mixture of oleylamine and 1-octadecene as a solvent heated up to 310 °C. As a result amorphous germanium nanoparticles were obtained with an average diameter of about 28 nm.[23] Gerung *et al.* described the synthesis of germanium nanocrystals by hot injection method using silylamido-based germanium precursor germanium (II) bis[bis(trimethylsilyl)amide].[24] Such precursors are quite easy to use because they will not give any potential halide contaminations as germanium chlorides or iodides. Moreover amido ligands are quite labile and in some cases thermal decomposition occurs at relatively low temperatures. This particular synthesis was performed at 300 °C in oleylamine as a solvent, which acts also as a capping agent. The average size of germanium nanocrystals is 7 ± 4 nm and 95 % of all particles are less than 8 nm.

Metallic seeds are essential for the synthesis of elongated germanium nanostructures as they allow for the SLS growth mechanism to perform, which in turn leads to controlled growth of crystalline nanostructures. Varying parameters of the synthesis using the metallic catalyst seeds one can control size, shape, size distribution and crystallinity of nanomaterials.[25] For the synthesis of germanium 1D nanostructures Au,[26-28] Ag,[29,30] Bi,[31,32] Ni,[33-35] Cu[36,37] and Mn[38] nanoparticles can be used.

1.3. TIN NANOPARTICLE SYNTHESIS

Tin, a heavier homologue of germanium, has a relatively low melting point of 231.9 °C for bulk material and this value can decrease with the particle size. Tin also forms an eutectic

point with germanium at 231.1 °C.[39] This makes tin a very beneficial material for germanium nanostructures synthesis.

Wang *et al.*[40] reported a method of bismuth nanoparticles synthesis that Korgel and co-workers adapted for Sn nanoparticles synthesis.[41] This hot injection method is based on thermal decomposition of the organotin precursor: tin (II) bis[bis(trimethylsilyl)amide] in a mixture of diphenyl ether as a solvent and poly(vinylpyrrolidonehexadecene) copolymer (PVP-HDE) as a surface modificator for Sn nanoparticles. Metal silylamide precursors have several advantages that were described in the previous chapter. The main advantage is reported decomposition at 180 °C over time. The obtained tin nanoparticles have an average diameter of 8 nm, so that they can be used as catalyst seeds for nanowires synthesis.

Another hot injection method was reported by Kravchyk *et al.* using tin amide as a precursor but oleylamine as a solvent and primary capping agent.[42] Tin nanoparticle formation proceeds through a reduction of the precursor with borane *tert*-butylamine complex acting as a reducing agent. As a result monodisperse tin nanoparticles were obtained with size over the range 9 – 23 nm. Although there are many reports on synthesis of polydisperse tin nanoparticles,[43] the synthesis of monodisperse sub-30 nm tin nanoparticles is quite demanding. The synthesis technique requires a relatively low-temperature, because tin starts to melt at 231.9 °C. Watanabe *et al.*[44] reported a low temperature reduction of $SnCl_2$ using tetrabutylammonium borohydride (TBBH, $N(C_4H_9)_4BH_4$) as a reducing agent. The obtained nanoparticles are in the size range 9 – 83 nm depending on the concentration of the precursor in the solution and the reaction temperature that varies between 0 °C and 70 °C.

Microwave-assisted synthesis is considered to be one of the most convenient, efficient and rapid methods in order to produce different nanomaterials. The utilization of microwave heating allows the synthesis of monodisperse, uniform, high-purity nanomaterials of controlled size. Microwave heating has already been utilized to synthesize different metallic nanomaterials such as Ni, Cu, Pt, Ru, Au, Ag, ZnO and other nanoparticles nanobelts, nanorods, nanowires, nanoclusters etc.[45-50]

Microwave heating is completely different from the conventional procedure. While the conventional heat comes from the outer sources and is transferred to the sample through convection, radiation or conduction, the heating process using the microwaves heats the inner part of the sample acting on the molecules.[51] The microwaves interact with polar molecules or charged particles and as a result they start to migrate or rotate. This leads to further polarization, where the molecules change direction with the frequency of about $2.4*10^9$ times per second. Rotating with such frequency causes the warming because the molecules in a liquid or semi-solid state cannot respond to such changes of the field, so the energy releases in form of heat.[52] Different thermal and non-thermal effects can be observed during the process of microwave irradiation. The effect of rapid heating depends on the polarity of the solvent and the reactants: the more energy they absorb the faster the heating.[53] Dipolar polarization that occurs during the interaction of microwaves with the molecules makes the whole microwave-induced reaction process more organized and hence the entropy contribution increases. The effect of decrease in the activation energy occurs according to the second law of thermodynamics with increasing entropy. Lewis *et al.* and Majetich *et al.* reported the experimental evidence of this process.[54,55] Thus, due to these effects, the microwave heating allows for using the energy with higher efficiency without loss of the heat due to thermal conductivity processes. An inverted temperature gradient is produced by creating the heat within the substance, which means that the

sample is heated more towards the center of the sample and less towards its external parts. Some experiments also claim the enhancement in the diffusion processes due to electromagnetic fields that can also increase the reaction rate.[51,56] The utilization of the microwaves can save much energy and time and hence the lower costs of the synthetic process.

There are different types of the microwave ovens present on the market. The electromagnetic spectrum of the microwaves varies between 300 MHz and 300 GHz. The most commonly used frequency for the chemical synthesis is 2.45 GHz. Microwave ovens and reactors usually operate with a power of 300-1100 W. The temperature range of a typical microwave reactor does not exceed 300 $^\circ$C.[57]

1.5. FUNCTIONALIZATION

In order to use germanium nanomaterials for various applications one needs to reach a certain level of chemical and electronic stability. The stability of the surface of germanium nanoparticles as well as for the nanowires is crucial for applications such as chemical and biological sensors, as they are in direct contact with the environment. For the applications in electronic and other devices it is important for germanium nanomaterials to be stable, not only chemically but also mechanically, i.e. nanoparticles or nanowires should not agglomerate nor aggregate.[58]

A layer of oxide is formed on the surface of germanium as well as many other metals. Some elements such as Si or Al have very stable oxide layers. The Ge/GeO_x layer, in its turn, dissolves in water forming germanium hydroxide $Ge(OH)_4$. The formation of $Ge(OH)_4$ proves poor chemical stability of Ge to the atmospheric conditions, which makes it impossible to use in field-effect transistors and other electronic devices.[58] The best way to maintain the stability of the surface is to use chemical passivation.

The surface of germanium nanostructures can be passivated with different classes of organic and inorganic compounds. Holmberg *et al.* reported in his paper a passivation of germanium nanowires using C_6, C_{12} and C_{18} alkenes in order to avoid corrosion processes.[59] The most commonly used class of substances for germanium nanostructures passivation is long chain alkanethiols as they provide very high stability from oxidation, hydrolyzation and aggregation processes. Yang *et al.* as well as Holmberg *et al.* have proven the stability of germanium nanowires in air when the germanium surface was treated with long-chain alkanethiols such as 1-dodecanethiol, 1-hexadecanethiol or 1-octadecanethiol.[59,60] Yuan *et al.* used dodecanethiol-passivated Ge nanowires for lithium-ion anode fabrication. Such nanowires showed superior electrochemical performances and reversible capacity. The charge/discharge capacity of Ge nanowires is two times higher than the graphite reference.[61] Collins *et al.* reported the passivation of the surface of germanium nanowires using hydrogen and halogen elements.[62] They discovered the formation of GeH_x mono-, di- and trihydride species on the surface using aqueous HF solution. The stability of nanowires in that cases strongly depends on if they were passivated during the synthesis process or afterwards.[63] For halogenation of the surface of Ge nanowires aqueous halogenic acids solutions (HCl, HBr, HI) are used. Halide-passivated Ge nanowires have greater stability to the ambient conditions with respect to H-terminated surfaces. The stability of the surface also increases with increasing molecular weight of the halogen species.[64] The passivation with hydrogen, halogens or alkanethiols can also be used as the first step for further functionalization of the surface with organic compounds for various applications.[65-69]

1.6.1. POWDER XRD

One of the most common techniques used for investigation of the crystal structure of compounds in a solid state is considered to be the X-ray diffraction. Amorphous materials or liquids have a degree of internal order only of few atoms or molecules. Interference effects between the wavefronts from neighbouring atoms randomly situated in the space result in a continuous scattering pattern of limited use. Crystalline structures give a discontinuous scattering pattern due to their long-range order, which depends on their relative positions and scattering powers of different atoms. This way, crystals provide an excellent diffraction grating for x-rays.[70]

An X-ray diffraction pattern of a single crystal occurs in form of a series of regularly spaced spots registered on a photographic film. Their positions depend on the size of the unit cell and the crystal orientation. In 1913 Bragg demonstrated that X-rays of a certain wavelength at different diffraction angles can result in the constructive interference. It occurs only when parallel diffracted waves show a path difference of $\lambda(2\pi)$. The constructive interference occurs in form of the scattering maxima depending on the angular distribution. It can be calculated by considering the diffraction process to require the geometrical conditions for reflection on a series of lattice planes (Figure 1). The Bragg equation (Eq.1):

$$\lambda = 2d_{hkl} \sin \theta, \qquad\qquad \text{Eq. 1}$$

where λ is x-ray wavelength, d_{hkl} is the interplanar distance and θ is the Bragg angle (Figure 1). The intensity of a Bragg reflection depends on the scattering powers of the atom and its relative position. The atomic scattering factor f measures the scattering pattern of the electron cloud of the atom in the unit cell. It is the Fourier transform of the atomic electron density. The atomic scattering factor depends on a wavelength, scattering power of the atom for a zero Bragg angle, number of electrons in the atom, their distribution and a temperature (Debye-Waller) factor that describes the attenuation of the X-ray scattering due to the thermal motion.[70] Theoretically, it is possible to measure the reflexes in the 0 – 180° angle range. In the range starting from 70° there are still some diffraction maxima that arise, but the intensities of reflexes decrease with increasing Bragg's angle. It is closely connected with the atomic scattering factor, which decreases with an increasing Bragg's angle.[71]
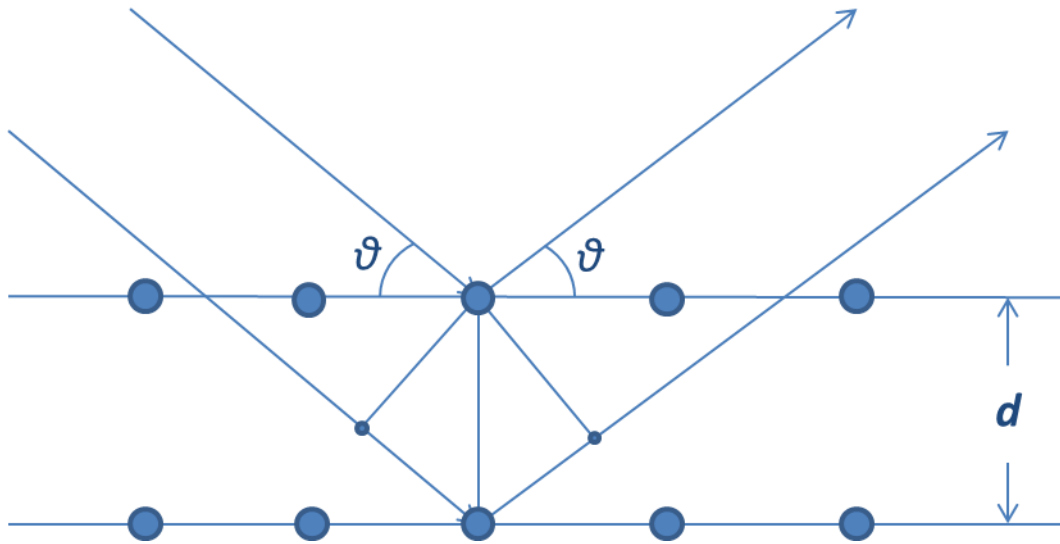
Figure 1: Schematic representation of Bragg's law.

Diffraction studies of powder samples are performed using a conventional sealed X-ray tube and a crystal monochromator that is used to obtain monochromatic x-rays. In a powder sample, there are a large amount of crystallites in the sample which means all the

crystallite orientations will surely be present, so that the Bragg's conditions could be fulfilled and the signal could be registered on detector.[70]

The diffraction pattern for a substance is characterized by the angular position (2θ), symmetry relationships and the intensities of the Bragg reflections. Normally the diffraction pattern consists of two types of signals: the diffraction maxima (reflexes) which are slightly raised by a background. The diffraction maxima are the cause of crystalline structure of a specimen and the background arises from the diffuse diffraction of the primary X-rays on air, diffractometer parts or also the specimen. There is a set of information about crystal structure of the specimen, which can be obtained from the diffraction pattern through the specific sequence of reflexes, their definite width and especially through their different intensities. Reflexes occur only at a certain, discrete diffraction angle 2θ whilst the background is a continuous function of an angle 2θ.[71]

The diffraction pattern of a crystalline phase can provide some further characteristics. From the Bragg's angle values one can determine the size of a primitive cell and lattice parameters. From the intensity of a diffraction maximum it is essentially possible to define the crystal structure of a compound and a crystallite size from its width. The crystallite size can be calculated by means of Scherrer equation (Eq. 2):

$$\tau = K\,\lambda/\beta\,\cos\theta, \hspace{4cm} \text{Eq. 2}$$

where τ is the crystallite size, λ – incident beam wavelength, K – crystallite shape factor, θ – Bragg's angle and β is the line broadening at half the maximum intensity (FWHM).[71]

In case of the amorphous material its diffraction pattern looks like one wide amorphous hump without any maxima. If there is more crystalline phases in one specimen the diffraction pattern would look like sum of the diffraction patterns of each crystalline phase.

As far as the intensity is concerned, the more quantity of one phase is present in the specimen, the more contribution of this phase will be noticed in the diffraction pattern.[71]

The scheme of a powder diffractometer is shown in Figure 2. The sample holder can be rotated about an axis normal to its plane during the measurement in order to maximize the randomness of orientation of crystallites. The line focus of the X-ray tube and the exit slit of the diffractometer are constrained to lie on a circle, so as to be equidistant from the sample holder, the surface of which is tangential to the circle. A bent crystal monochromator – adjusted to fulfil the Bragg's condition for a strong reflection *hkl* – is employed to focus the X-rays onto the entrance slit. Divergence of the incident and diffracted beams within the diffractometer is restricted by passing these through a series of thin Soller slits. The detector rotates at a constant speed around the center of the sample and the sample holder rotates at half detector's speed in order to maintain the geometry of the focusing circle during the registration of the diffraction pattern.[70]
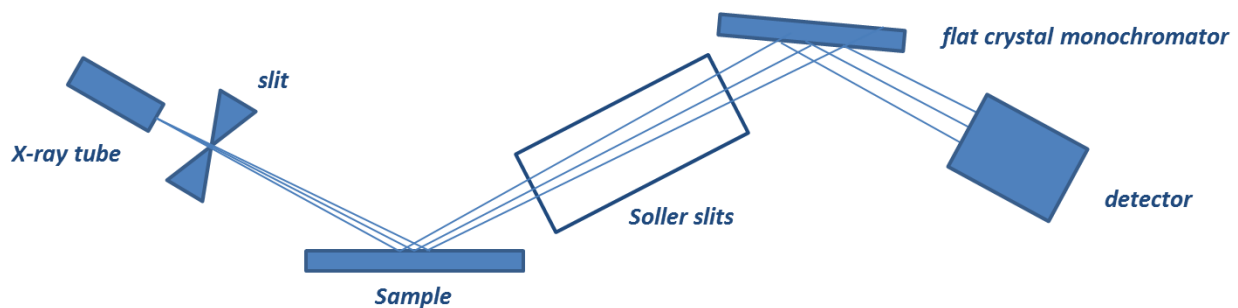
Figure 2: Schematic representation of a powder diffractometer.[72]

Dynamic light scattering is one of the most common techniques to determine the particle size. This method is also known as Photon Correlation Spectroscopy. This method is based on the Brownian motion of the particle in liquid solution. The incident light beam hits the particle and deflects its straight path.[73]

There are different techniques to study the light scattering. Static light scattering is the elastic interaction with the matter, i.e. no wavelength changes take place. Due to the Brownian motion of the particles the scattered light fluctuates and the light intensity changes. This phenomenon is called a light intensity fluctuation. Static light scattering experiment is based on the determination of the light intensity at a given angle. The fluctuating intensity is averaged over a long time scale in relation to the period of time needed for the fluctuation. The measurement of angular and concentration dependence of the intensity of the scattered light gives information about molar mass and size of macromolecules. Raman scattering occurs at a wavelength different from that of incident light and it provides the structural information of the compound.[74]

Dynamic light scattering occurs at the same wavelength of the incident light, but in this case the fluctuations are studied instead of average intensity. The fluctuation is over extremely short time intervals, so the phenomenon of dynamic and static light scattering is practically the same differing only in the way of collecting data. The light beams scattered at a given time by different particles are, to a certain extent, phase shifted and mutually interfere. The interference can be either positive or negative depending on the mutual position of scattering particles. After some time the particles move to another position and the intensity of scattered light changes. The fluctuation of the intensity of the scattered light reflects the motion of the scattering particles. In case of large particles that move slowly, the fluctuation of the light intensity is slow too, while for small particles moving rapidly the

light intensity fluctuates rapidly too. Thus the fluctuation delivers the information about the particle's size.[74]

In order to transform the information about the moving particles a correlator is used. A correlator is an electronic device that compares two signals coming from the detector using Fourier transformation. It transforms the intensity fluctuation into the intensity autocorrelation function, which expresses the similarity of the signal with itself. It represents a certain probability that after time delay the intensity of the scattered light will be the same as in the initial time. At short time delays the correlation is high because the particles do not have enough time to move to another position. The longer the time delay the lower the correlation. The correlation decreases exponentially until a certain time delay, where no correlation between the scattering intensity at the initial and end time is observed. A faster delay corresponds to smaller particles, while a slower delay indicates the larger ones. The normalized intensity autocorrelation function is defined as follows (Eq. 3):

$$g(\tau) = \{I(t)I(t+\tau)\} / \{I(t)\}^2 \qquad \text{Eq. 3}$$

where $I(t)$ is the detected intensity as a function of time t, $\{I(t)\}^2$ is the average scattered intensity squared, τ is a delay time, and the brackets indicate averaging over all t. For a monodisperse system the normalized autocorrelation function (Eq. 4) would be:

$$g(\tau) = 1 + \beta e^{-2D\mu^2 \tau} \qquad \text{Eq. 4}$$

where $\mu = 4\pi \sin(\theta/2) / \lambda$, D is the translational diffusion coefficient, β is the signal amplitude of the autocorrelation function, λ is the wavelength of light in a given solvent, and

θ is the detection angle with respect to the direction of the incident beam. One can determine the hydrodynamic radius (Eq. 5) by assuming that the particle's shape is a sphere and by using the diffusion coefficient. The hydrodynamic radius refers to the radius of a hydrodynamically equivalent sphere with the same diffusion coefficient:

$$R_h = kT / 6\pi\eta D$$
<div align="right">Eq. 5</div>

where k is Boltzman's constant, T is the absolute temperature and η is the solvent viscosity. The diffusion coefficient and the hydrodynamic radius can be accurately determined only for the diluted solutions, where there are hardly any interactions between the particles over the selected period of time.[74]

Although dynamic light scattering is considered to be an absolute method for the determination of hydrodynamic radius, (Eq. 5) the measurement of polydisperse systems is limited with the possibility to characterize the size distribution. In a polydisperse system the autocorrelation function (Eq. 4) has two decays; one representing smaller and one representing larger particles. The results from the batch DLS are expressed using a diagram with several peaks. The number of these peaks can serve as an estimation of the size distribution, although it is not the true distribution. For instance, if there are only three peaks presented in the diagram, it does not mean that there is a mixture of particles of only three distinct sizes presented in the solution. The results can also be recalculated into mass % size distribution and number % size distribution of all the particles in the solution.[74]

The set-up of dynamic light scattering experiment is illustrated in Figure 3. The red light laser (675 nm) passes through a collimator lens and then reaches the sample in the form of a solution. The scattered light is collected by an optical fiber, detected by a photomultiplier and analyzed by a correlator that measures the autocorrelation function of the intensity. As

illustrated in Figure 3, there is another collimating lens before the photomultiplier. The use of both the collimating lenses is essential: the first lens allows focusing the beam into the cell, while the second lens is used to get the right amount of the scattered light into the photomultiplier. The photomultiplier is placed at a scattering angle of 90 degrees in order to neglect the nonlinearity of the line width with the scattering angle. Finally the photomultiplier will transform the intensity variation into a voltage variation that is proportional and send it to the correlator.[73]
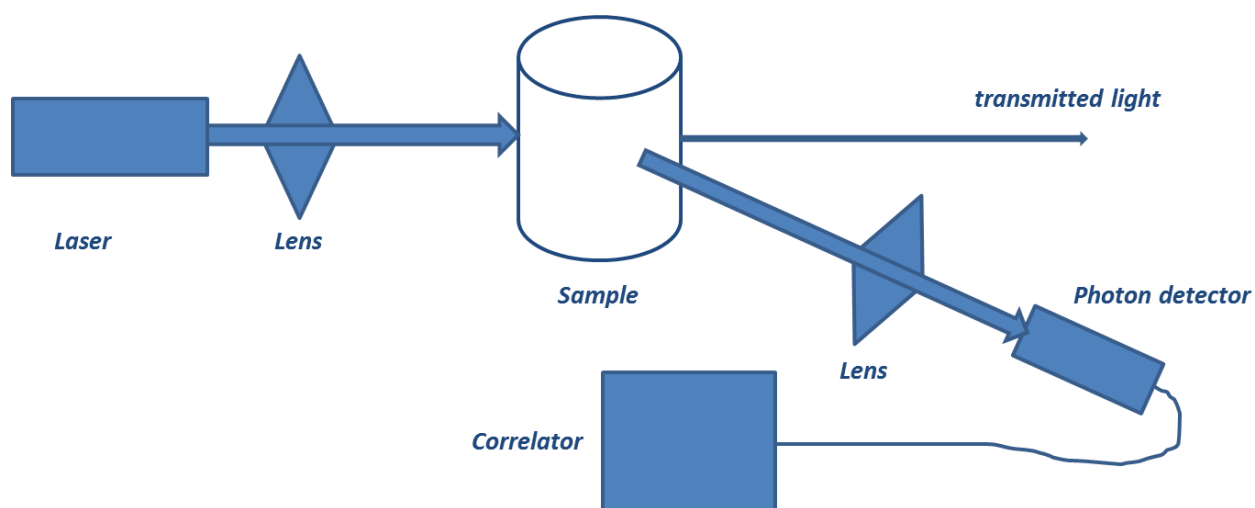
Figure 3: Dynamic light scattering experiment set-up.[75]

1.6.3. THERMOGRAVIMETRIC ANALYSIS

Thermogravimetric analysis (TGA) is an analytical technique used to determine a thermal stability and a fraction of volatile components of a material. A typical procedure consists of

the registration of the weight change as the specimen is heated.[76] The experiment is carried out either under inert atmosphere or under synthetic air conditions. During the experiment the sample is heated up to 900 °C, but the maximum temperature is selected so that the sample's weight stays stable. The sample can be heated using different time-temperature programs such as heating at constant rate, isothermic or gradually isothermic heating.[77]

During heating different chemical and physical processes take place. Among the physical ones there are gas adsorption, gas desorption, vaporization *etc.* Decomposition, chemisorption and oxidation are chemical processes which are strongly affecting the sample mass change during the experiment.[77]

As illustrated in Figure 4, a TGA consists of a sample pan that is placed on a precision balance. The balance together with the sample pan is situated inside a furnace and is heated or cooled during the experiment. The mass change of the sample is monitored and registered during the experiment. Either inert or reactive gas is used as a sample purge gas that controls the sample environment during the measurement. It flows over the sample and exits through an exhaust.[78] Different sensors can be used in order to increase the accuracy of the balance. Some of them use an electro-, optical device with a shutter attached to the balance beam.[79] With the high precision of these instruments one can quantify loss of water, loss of solvent, loss of plasticizer, decarboxylation, pyrolysis, oxidation, decomposition, weight % filler, amount of metallic catalytic residue remaining on carbon nanotubes, and weight % ash in the sample.[78] It is worth mentioning that the lower the heating rate the more accurate are the results.
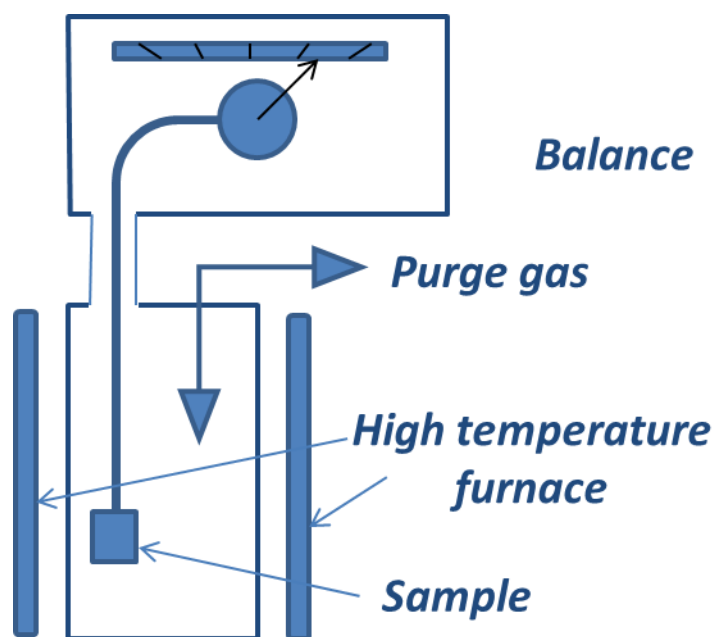
Figure 4: A TGA instrumentation scheme.[79]

The measured weight loss curve gives information on changes in sample composition and sample composition in general, weight percentage of each component in the sample, thermal stability of each component and kinetic parameters for chemical reactions in the sample. A schematic illustration of a thermogravimetric curve of a multicomponent sample is shown in Figure 5. Three important parameters could be obtained from this curve. The residual mass indicates the weight % of the most stable component of the sample in its oxidized form in solid state. Three areas with rapid mass loss give us the information about other components and their mass content in the sample or in case of one component system three steps of the substance decomposition. It is also possible to obtain the decomposition/oxidation temperature of each component in the sample using the extrapolation method as shown in Figure 5: the first line continues the plain part of the curve and the second line continues the drop part of the curve, the point two lines cross is the onset temperature.
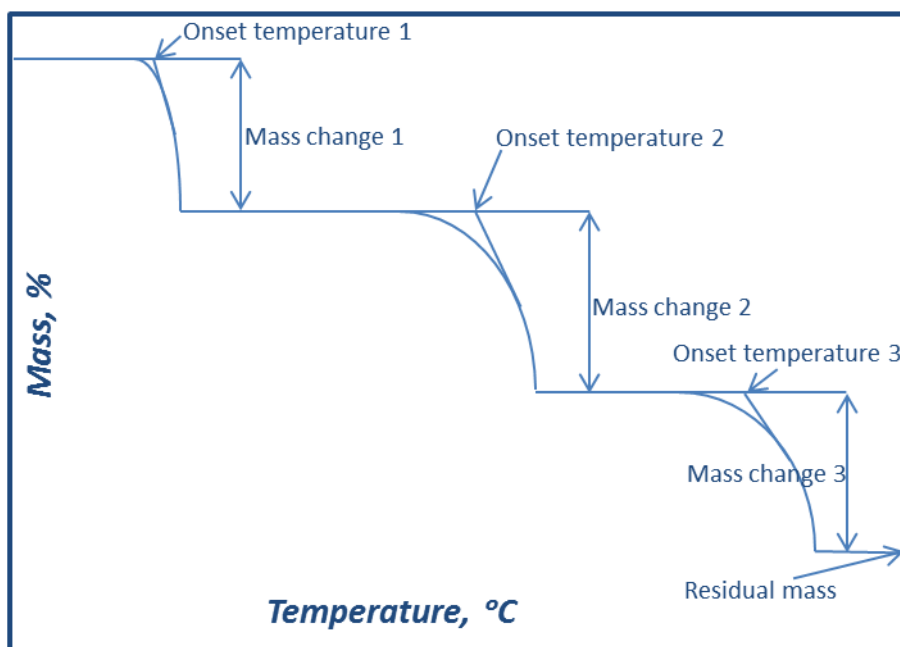
Figure 5: A schematic representation of a typical TG curve of multicomponent sample.[80]

Thermogravimetric analysis has many other important applications. For instance, it can be used to measure evaporation rates of volatile emissions of liquid mixtures. It also allows for the analysis of reactions with air, oxygen, or other reactive gases. It helps to determine the purity of a mineral, inorganic compound, or organic material and also to distinguish different mineral compositions.[81]

1.6.4. SCANNING ELECTRON MICROSCOPY

Interactions of electrons in the energy range between a few eV and hundreds of keV with the matter provide the important information about surface of the sample. When an electron hits

the specimen it can either interact elastically or inelastically. Elastic scattering leads to deflection of transmitted and reflected electrons and diffraction phenomena. Inelastic processes lead to excitation of electronic states and plasmons. Both elastic and inelastic processes cause the broadening of the finely focused electron beam. The elastic interaction of electron with an atom has the Coulomb interactions as its origin and results in the scattering phenomenon at the atomic nuclei. The scattering at nuclei occurs with much higher probability in small angles (2-3°). When the electron hits the specimen and experiences multiple scattering events it can be backscattered from the specimen with certain probability. This effect is being used for analyzing both backscattered and transmitted electrons. The backscattered electron intensity is measured as a function of the position of a finely focused electron beam and it provides the information about the microstructure of the specimen. As a result of the inelastic scattering process secondary electrons (SE) are ejected from the k-shell of the specimen's atoms. SE have low energy and the probability to be detected is higher, when the angle of incidence increases. The signal from the SE is displayed in the form of the two-dimensional intensity distribution as a function of the position of the electron beam. These two processes are crucial for SEM.[70]

SEM is the most widely used techniques among other electron beam instruments for the routine imaging and elemental analysis. It has a wide range of imaging modes and high spatial resolution. The sample is probed by a beam of electrons scanned across the surface. Each radiation type coming from the specimen is collected with an appropriate detector the signal is then amplified, converted into an electric signal and displayed on the computer console.[82]
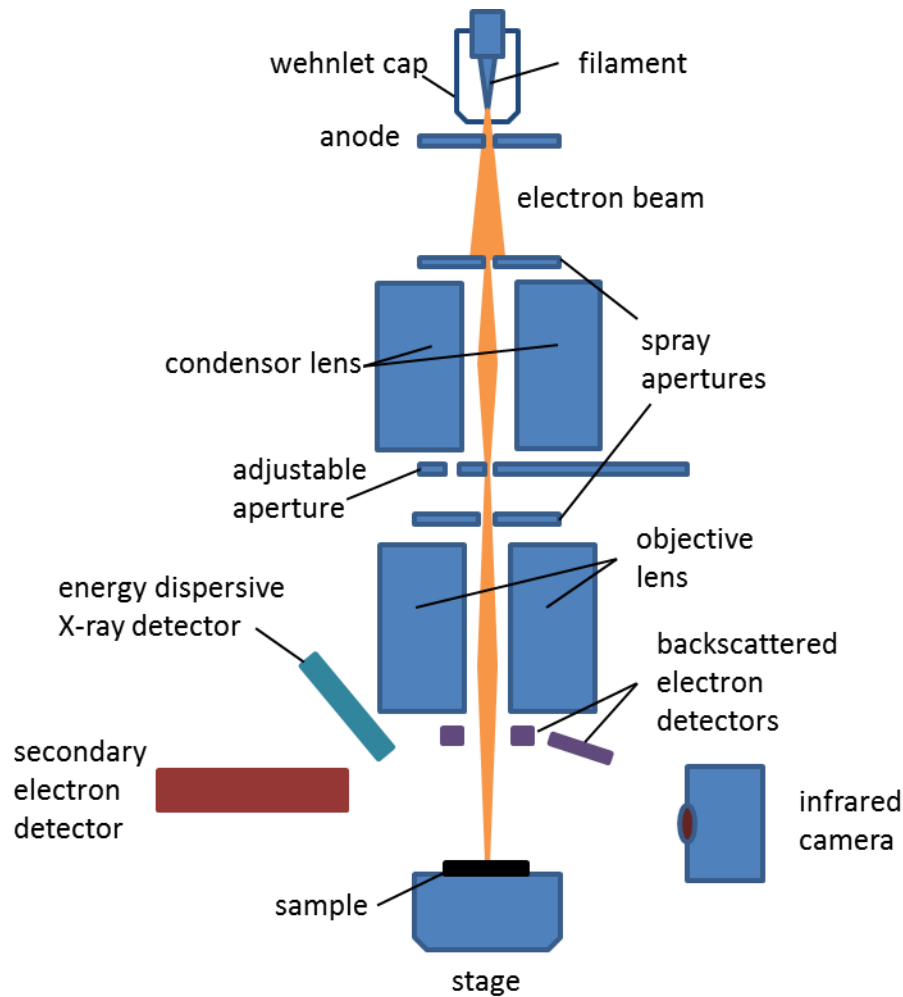
Figure 6: Schematic representation of a SEM instrument.[83]

A SEM machine consists of an electron source, detectors, scanning, processing, and computing systems (Figure 6). SEM is operated in vacuum in order to minimize the interaction of the electron beam with the air molecules. An electron gun produces the electron beam due to the process of thermoemission from tungsten or lanthanum hexaboride cathodes. The electrons are then accelerated to the anode ring and usually reach the energy of 500 – 30000 eV. The beam of electrons leaves the gun and is focused towards the specimen with one or more condenser lenses. Condenser lenses create an electromagnetic

field, which helps to focus the electron beam due to the Lorentz force. The scanning system is usually incorporated in condenser lenses, thus changing the electromagnetic field helps not only to focus the electron beam, but also to direct the beam towards the specific point of the specimen. The scan pattern produced on the specimen is usually either square or rectangular in shape. For instance, it is made up of 1000 horizontal lines each containing 1000 individual scanned points (pixels). As a final picture one gets the square frame, which contains 10^6 pixels. The detector system includes such detectors as a secondary electrons detector, backscattered electrons detector and a detector for fluorescent X-rays.[82]

As the electron beam travels through the specimen, a loss of kinetic energy due to inelastic scattering ionization of the electronic levels takes place. Thus secondary electrons (SE) with low kinetic energies about 10 eV are generated. The SEs generated near the surface of the specimen have a chance to escape from the specimen, be accelerated with a potential of several hundred volts and be detected with a scintillator crystal producing photons. The signal is then being enhanced with a photomultiplier tube and amplified. SE imaging is the most common mode of operation of the SEM. The utility of this mode is the result of such factors as the easiness of collecting SE. SE provide information exclusively from the surface of the specimen and the SE image has a spatial resolution of 1 nm or better under properly optimized conditions. The ability to view topographic detail occurs because the yield of secondary electrons varies with the angle between the incident electron beam and the local surface normal. Areas which are at a high angle to the beam are bright compared to those which face the beam normally.[82]

Backscattered electrons (BSE) are the incident electrons which have been scattered through angles approaching 180º within the sample, and consequently leave the specimen again.[82] The BSE are then detected with a scintillator, which emits light in a visible range when struck by electrons. The scintillator is usually made of Ce-doped yttrium-aluminum garnet (YAG) since such materials have a low decay time, which means that the scintillator stops emitting light a few nanoseconds after the last electron hit it. Once the signal is converted into the visible light, it is amplified by a photomultiplier tube.[84] The detector is

usually placed above the specimen right after the exit of the electron beam from the objective lens (Figure 6). The BSE have energies of a similar order to the incident beam. Unlike SE coming from the surface, BSE emerge from the volume. The BSE yield depends on the atomic number of the specimen.[82] The atomic number contrast or Z-contrast at a SEM image is generated by the BSE scattered from atoms of different types. The signal coming from the heavier atoms creates brighter regions with respect to the BSE coming from areas with the lower average atomic number.[85] Thus BSE reveal the presence of numerous precipitates, while SE image shows homogeneous specimens. It is a quick method to examine the qualitative distribution of the elements in the specimen. The BSE image shows heavy metals as bright spots against the dark background of the carbon matrix. The BSE image is not the most accurate technique for elemental mapping, because there are an infinite number of ways to achieve the same average atomic number combining different elements. If the incident electron beam enters the crystalline specimen at a random angle the backscattering will occur in the normal way, but if it is angled along the symmetry direction it penetrates more deeply, and as a result the yield of BSE will be reduced. Thus the crystalline nature of the sample using the BSE could be detected. [82]

When an electron hits the atom it might cause the electronic excitation of core levels producing ions in a highly excited state, because the hole is situated in an inner orbital. In order to gain more favorable energetic state an electron from upper level "falls" onto the lower level. The energy difference gained produces an X-ray photon. Energy-dispersive X-ray (EDX) and wavelength-dispersive X-ray (WDX) spectrometers are used to measure the energy and intensity of the characteristic X-rays. The EDX consists of a semiconductor detector. Once photons hit the detector they are converted into electrical pulses, the intensity of which is proportional to the energy of the photons. The EDX spectrum shows a resolution of approximately 140 eV at medium X-ray energies. The WDX consists of a diffraction crystal. It selects a particular wavelength of the spectrum and when the Bragg condition is fulfilled the reflected radiation is detected and quantified with ionization or scintillation detectors. The WDX has much higher resolution of about 5 eV and a better

signal-to-noise ratio than EDX, but only allows for selective analysis of various elements prior to the relatively long period of time needed for the measurement of one wavelength.[70]

1.6.5. TRANSMISSION ELECTRON MICROSCOPY

Transmission electron microscopy (TEM) is a microscopy technique, which detects the transmitted electron beam after it undergoes a series of elastic and inelastic scattering events in order to obtain the morphological and structural information about the specimen. A scheme of a transmission electron microscope is illustrated in Figure 7. The electron source is the same as in the SEM. It is an electron gun, which is operated at intensities range of approximately 200 keV. The electrons emitted by the source are accelerated and collimated with help of electromagnetic condenser lenses which are the same in SEM. TEM must also be operated in vacuum. In order to operate in transmission mode the specimen should not be thicker than 100 nm. TEM can be represented as a three-lens microscope. An objective lens, an intermediate lens and a projector lens lead the image formation process. By virtue of all three lenses the system could be easily switched between the imaging and diffraction mode, change magnification, resolution etc. As the electron beam is scattered by a specimen an image in the image plane of the objective lens is formed. The intermediate lens is focused on the image plane of the objective lens, which allows for one to select one area that will be magnified by the intermediate lens. Thus an intermediate image in the image plane of the intermediate lens is formed and is the object for the projector lens. After passing through the projector lens the final image on a fluorescent screen is formed.[82]
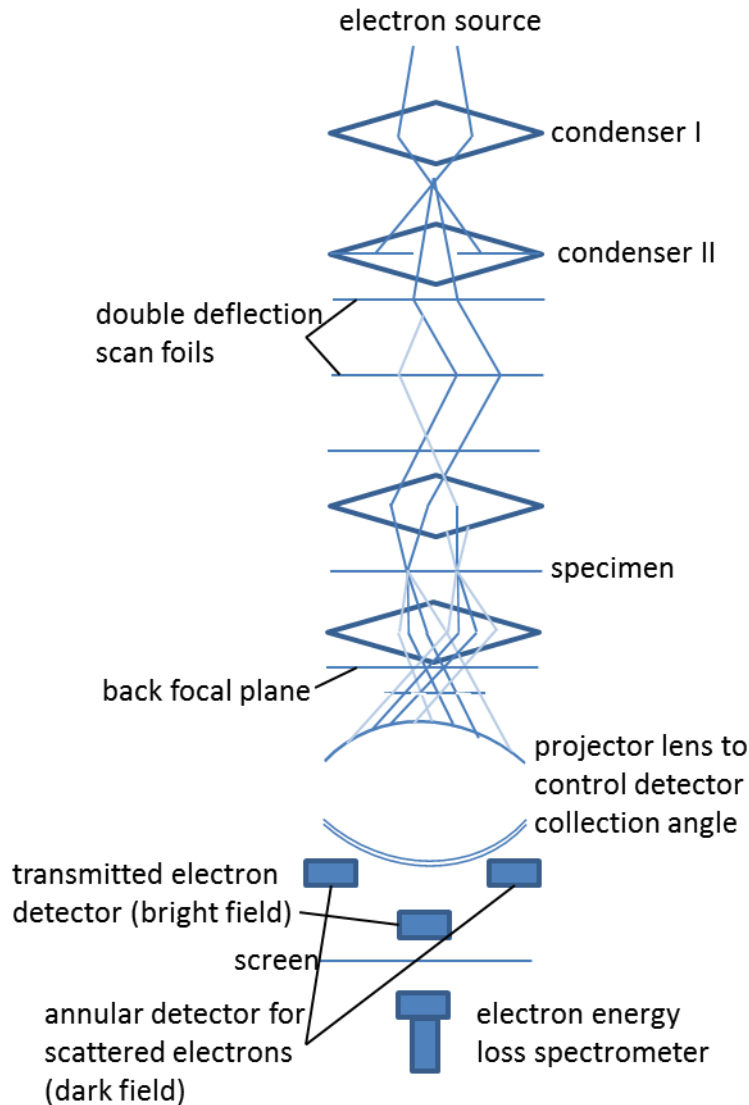
Figure 7: Schematic illustration of transmission electron microscope.[70]

TEM has several working modes and types of imaging. When the electron beam hits the crystalline specimen it can undergo diffraction phenomenon. Scattering that electron experiences under Bragg-angle conditions helps to obtain the diffraction pattern which can be measured either in reflection or in transmission. The diffraction patterns of polycrystalline materials present in form of concentric rings. Amorphous material shows

diffuse circular halos, while the diffraction pattern of a single crystal occurs in the form of periodically ordered dots (Figure 8). From the spots and ring patterns lattice spacing (Eq. 6) can be obtained using the geometric relationship:

$$\lambda L = Rd, \qquad\qquad \text{Eq. 6}$$

where L is the distance between the sample and the observation screen, R is a radius of diffraction ring, λ and d are known from Bragg equation.[70] In the diffraction mode the intermediate lens is weakened and the focal lens is made larger, so that the focal plane of the objective lens coincides with the object plane of the projector lens. This way the diffraction pattern will be obtained on the fluorescent screen (Figure 7). The aperture placed close to the back focal plane allows for the beam to be either transmitted or diffracted.[82] The image intensity varies strongly depending on changes in the crystal lattice orientation angles. As the electron beam irradiates most of the specimen, the diffraction pattern will contain the electrons from the whole specimen. Generally this does not provide very useful information as the specimen will often be buckled. In order to obtain the needed information from a diffraction pattern, the electron beam will irradiate a selected area of the specimen (SAED). SAED patterns serve mainly to determine the crystal structure of nanodomain in a material.[86]
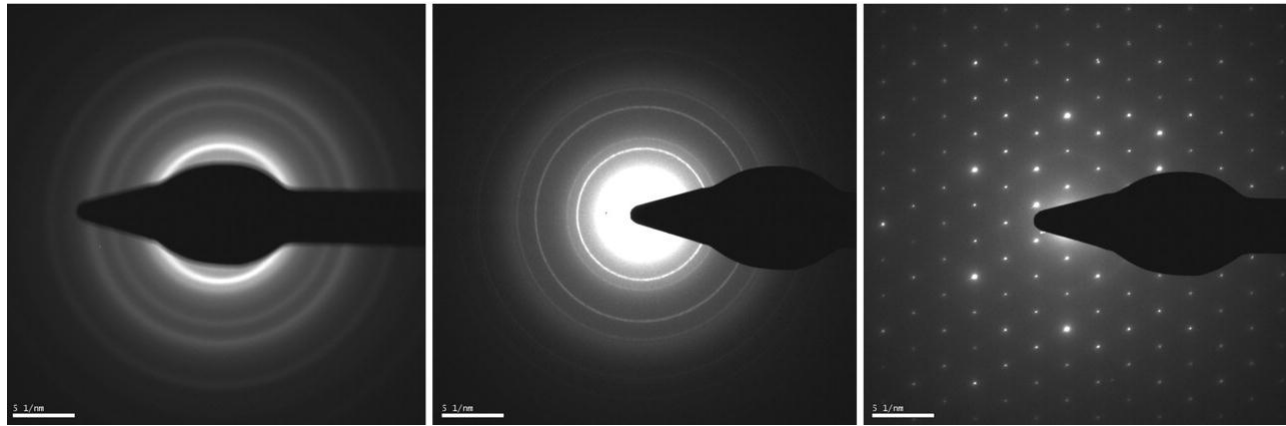
Figure 8: SAED image: polycrystalline (center), single crystal (right), amorphous (left).[87]

Once the SAED pattern is projected onto the screen it contains a bright spot of direct and some scattered electrons in the center of the image independent of the specimen's type. In order to form a TEM image one can either use the bright spot or the scattered electrons. Each option can be chosen either by inserting or removing an aperture into the back focal plane of the objective lens. If the direct beam is selected, a bright field (BF) image is obtained and if the scattered electrons are selected, the resultant image will be called a dark field (DF) image.[86] The magnification of such images can reach 100,000 times. One can change the magnification simply by adjusting the intermediate lens.[86] The DF imaging procedure is based on the detection of the transmitted electrons. When scattered from different atoms, the transmitted electrons result in a different yield. The electrons scattered from heavier atoms create brighter areas with respect to the signal coming from the lighter atoms. Thus, the transmitted electron DF image shows an atomic number-dependent contrast (Z-contrast) and allows distinguishing nanodomains with different atomic numbers. This effect represents a part of TEM imaging mechanism.[70]

The dominant inelastic processes are the excitation of vibrational states, plasmons and ionization. These effects come along with the energy loss of the electrons, causing distinct "absorption features" in the energy spectrum of the initial electron beam. This process is

the main principle of electron energy loss spectroscopy (EELS). The energy loss is due to ionization which allows for the qualitative elemental analysis. It is characterized by ionization energy of the particular core level.[70] EELS separates the inelastically scattered electrons into a spectrum, which could be elementally interpreted, quantified and combined with TEM images. The spectrometer consists of two parts; the first being an energy filter made into a magnetic prism tube with two poles that selects electrons of particular energy values. When the electromagnetic field of certain value is applied, electrons are deflected in accordance with Lorentz force. Only electrons with the certain selected energy could pass through the tube, while electrons with different energies would stick to a magnet. To gather a spectrum one needs to record the signal. This function fulfils a charge-coupled device (CCD). CCD is an array of metal-oxide-semiconductor (MOS) capacitors (pixels), which are electrically isolated from one another and can store charge generated by the electron beam. The collected charge could then be transferred to a digital camera producing an image or converted into an EELS spectrum. A typical EELS spectrum consists of two regions: low-loss and high-loss. The low-loss region provides information from the more weakly bound conduction and valence-band electrons, while the high-loss region contains information from the electrons more tightly bounded in the atom such as core-shell electrons and can also give details regarding bonding and atomic distribution. Usually the logarithmic graph is used in the spectrum because of the strong difference in intensities.[86] Different elements in a sample will interact differently with the electron beam resulting in different electron energies. These can be detected as a function of a thickness of the sample. EELS has, to its big advantage the potential to analyze elements with the low atomic number with good sensitivity, since the number of ionizations in the analytical volume determines the signal. The big disadvantage of this method is a poor signal-to-noise ratio, as the transmitted electrons lose the majority of their energy due to inelastic scattering processes. The signal-to-noise ratio can be improved when thinner samples (10-20 nm) are used. Quantitative evaluation of energy loss spectra has relative accuracy of 10-20%. Although the accuracy of this method is quite poor, it remains a good technique for the analysis of the atoms with low atomic number, as they have better signal-to-noise ratio with respect to heavier atoms.[70]

2. MOTIVATION AND RESEARCH GOALS

Germanium is a very important material in the semiconductor industry. Nanosized germanium has excellent semiconductor properties due to the quantum confinement effect. For instance, it has smaller band gap (0,67 eV in bulk Ge at 300 K), larger Bohr radius (approx. 12 nm) and higher electron and hole mobility with respect to the elemental silicon.[88] Moreover, Ge nanocrystals have a large absorption coefficient (2×10^{5} cm^{-1} at 2 eV) and a technologically important absorption spectrum.[89,90] Elemental germanium has a wide range of different applications. It can be used in optoelectronics, photovoltaics and, due to its nontoxicity, in biological cell imaging and labeling[91] as well as in photothermal therapy.[92] Ge can be used in optoelectronic devices such as photodetectors,[93] in field-effect transistors,[94] solar cells etc.[95]

Using germanium nanostructures has its drawbacks. For one, there are not so many synthesis routes developed for narrow size distribution, uniform shape, crystalline, elongated germanium nanostructures. The existing ones often demand high temperatures, expensive catalysts or reducing agents. Thermal decomposition of the organogermane precursors[96] in the microwave reactor seems to be an excellent option for that purpose and the thermal decomposition method does not require high temperatures or any reducing agent. The microwave reactor has its certain advantages. It consumes less energy with a higher efficiency, has high heating rate, and the procedure for using the microwave reactor is also very simple.[97] Using tin as a metallic catalyst seed in SLS grow mechanism is a good option for the reason that it has a low melting point and it also belongs to group IV.

This thesis focused on the synthesis and characterization of germanium elongated 1D crystalline nanostructures with the uniform shape and narrow size distribution. The first aim was to synthesize crystalline germanium nanostructures at a low temperature. The crystallinity of each sample was investigated by powder XRD technique. When the SLS

mechanism was fulfilled and crystalline structures formed, the next goal was to maximize the aspect ratio of germanium 1D nanostructures by varying the molar ratios of both precursors and also by using either different tin precursor or pre-synthesized tin nanoparticles. Ready-made tin nanoparticle can also be used for the purpose of being catalyst metallic seeds. All germanium nanostructures obtained were characterized by DLS and powder XRD techniques. DLS technique was used to form the general idea of the size and size distribution of the obtained nanostructures. The powder XRD was used to prove the crystallinity of the samples, their size and the crystal phase of the elements in the samples. The crystalline germanium nanostructures were then further investigated by SEM and TEM microscopy in order to obtain the image of germanium nanostructures geometry, aspect ratio and all the visual characteristics.

Therefore, the second part of the practical work for this thesis focused on finding and optimizing an appropriate synthesis route in terms of nanoparticles size, size distribution and appropriate capping agent that provides sufficient surface passivation for tin nanoparticles, and will not harm the further synthesis. The molar ratio between the capping agent and tin nanoparticles was investigated by TGA. Tin nanoparticles were also characterized by DLS in terms of their size and size distribution; powder XRD in terms of crystallinity and elemental analysis, SEM and TEM techniques in terms of size, crystallinity, and in order to obtain information on the materials shape and composition.

3. RESULTS AND DISCUSSION

3.1. THERMAL DECOMPOSITION OF GERMANIUM (II) BIS(BISTRIMETHYLSILYL)AMIDE

As it was mentioned before, the aim of this work is to synthesize crystalline elongated germanium nanostructures of uniform shape with narrow size distribution. Germanium nanostructures are obtained by the thermal decomposition of germanium (II) bis(bistrimethylsilyl)amide in the microwave reactor. The hot injection method reported in the article by Gerung and co-workers is taken as a base and adapted for the microwave reactor.[24] The detailed synthesis procedure is described in sections 5.4.1. and 5.4.2. After the purification DLS measurements of the obtained germanium structures are performed, which are shown in Figure 9. The reaction is performed at different temperatures for different periods of time such as at 240 °C for 10 minutes; at 260 °C for 10 minutes; at 200 °C for 30 minutes and at 220 °C for 30 minutes. From DLS numeric size distribution the growth velocity at different temperatures can be observed. Generally one can see that at higher temperatures or at longer periods of time the nanoparticles have grown bigger. The diameter of the particles grown at 240 °C for 10 minutes is 2.88 ± 0.04 nm while the diameter of the particles grown at 260 °C for 10 minutes is 22.4 ± 0.1 nm. The same tendency can be noticed for 30 minutes reactions, i.e. at 200 °C Ge nanoparticles diameter is 3.6 ± 0.2 nm and at 220 °C it is 26.2 ± 0.1 nm. The nanoparticles that have grown for 30 minutes are slightly bigger with respect to those with 10 minutes growth time, even if they have grown at lower temperatures. The reaction is also performed at 220 °C for 5 and for 10 minutes and at 200 °C for 10 minutes. The reaction at 220 °C for 10 minutes takes place as the colour of the solution in the end of reaction becomes dark brown. In two other cases the solution had become dark orange, which points on the fact that the precursor does not decompose completely in such a short time.
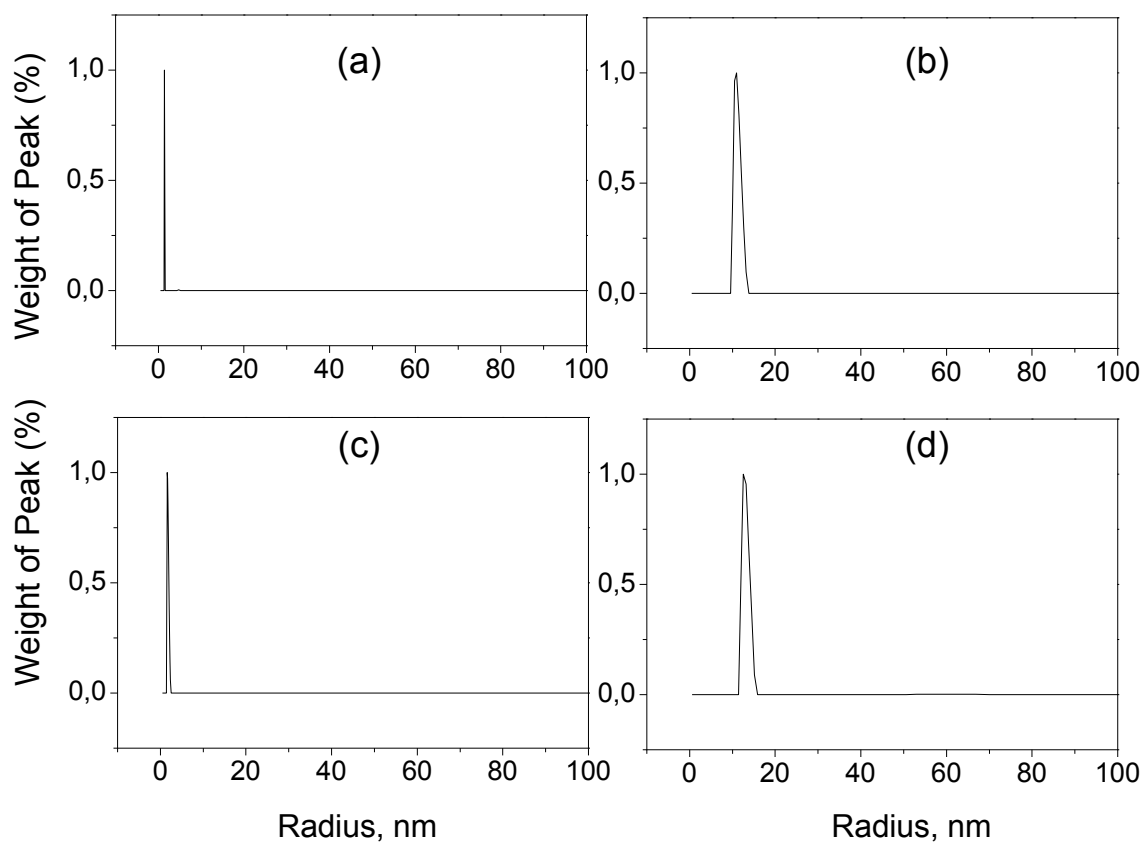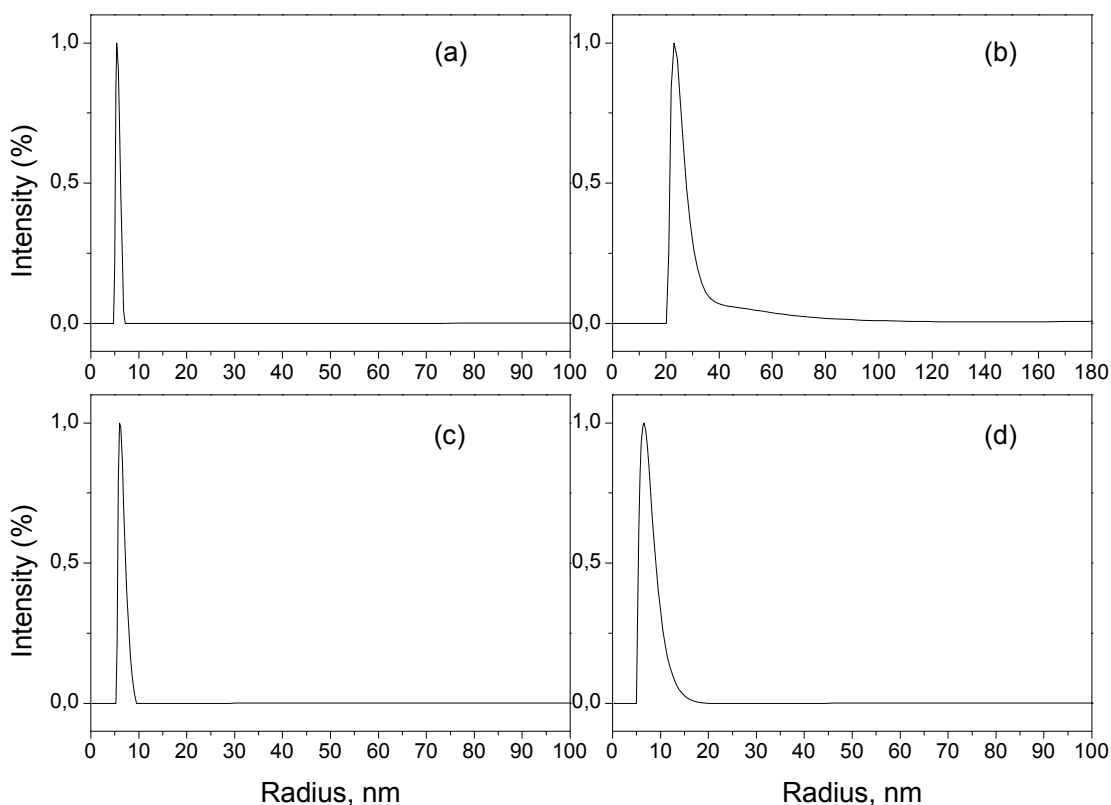
Figure 9: DLS of germanium structures synthesized at different reaction temperatures and reaction times: (a) at 240 °C for 10 minutes; (b) at 260 °C for 10 minutes; (c) at 200 °C for 30 minutes; (d) at 220 °C for 30 minutes.

After the purification the nanoparticles are stored in the glovebox and, in order to perform the powder XRD measurements, they have to be re-dispersed in n-pentane. The obtained Ge nanoparticles are capped with dodecylamine, which is used as a solvent during the synthesis process. Dodecylamine does not act as a strong capping agent. Thus, the nanoparticles form bigger agglomerates, which cannot be separated again even after placing them into the ultrasonic bath together with couple mL of dry toluene for two hours. So after the Ge nanoparticles are obtained the exchange process on the surface of Ge nanoparticles is performed. Dodecylamine is exchanged with a stronger capping agent 1-

dodecanethiol during the purification step. 1-dodecanethiol capped nanoparticles can very easily be re-dispersed in toluene as well as in n-pentane.

In Figure 10 one can observe the numeric size distribution of the obtained Ge nanoparticles capped with 1-dodecanethiol at different temperatures and reaction times. The nanoparticles obtained at 220 °C in 10 minutes reaction are 11.2 ± 0.2 nm in diameter. The 10-minute-reaction at 240 °C gives Ge particles 57.6 ± 0.8 nm in diameter. Meanwhile, the nanoparticles obtained during the 30 minutes reaction at 200 °C and 220 °C are 13.0 ± 0.2 nm and 14.8 ± 0.4 nm respectively.

Figure 10: DLS of germanium nanoparticles capped with 1-dodecanethiol synthesized at different reaction temperatures and reaction times: (a) at 220 °C for 10 minutes; (b) at 240 °C for 10 minutes; (c) at 200 °C for 30 minutes; (d) at 220 °C for 30 minutes.

In Figure 11 the powder XRD patterns of the obtained nanostructures are shown. The Ge reference is red. In all cases there are no traces of the crystalline Ge structure in any sample. The detailed information about Ge crystallographic structure is shown in Table 1. This fact brings us to the conclusion, that no non-metal seeded crystal growth is possible for germanium structures in such conditions and a metal catalytic seed is needed in order to perform an SLS mechanism and grow elongated crystalline structures.
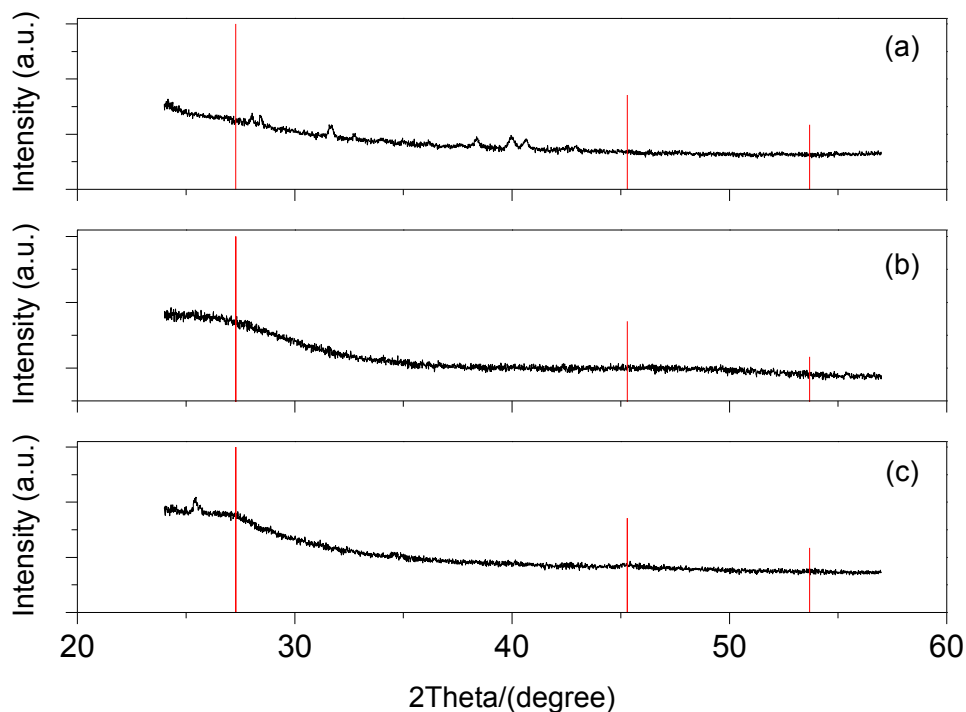
Figure 11: XRD patterns of germanium structures synthesized at different reaction temperatures and reaction times: (a) at 220 °C for 10 minutes; (b) at 200 °C for 30 minutes; (c) at 220 °C for 30 minutes (Ge 00-004-0545 - red).

Table 1: Crystal data of Ge and Sn.

Element

Germanium Ge (red references)	Reference code[98]			00-004-0545		
	Space group number			227		
	Space group			Fd3m		
	Crystal system			Cubic		
	a, b, c (Å)			5,6576		
	α, β, γ (°)			90,0000		
	Volume of the cell (10^6 pm^3)			181,09		
	Peak	*h*	*k*	*l*	d [A]	2Theta[deg]	I [%]
	1	1	1	1	3,26600	27,284	100,0
	2	2	2	0	2,00000	45,306	57,0
	3	3	1	1	1,70600	53,683	39,0
Tin α-Sn (blue references)	Reference code[99]			00-005-0390		
	Space group number			227		
	Space group			Fd3m		
	Crystal system			Cubic		
	a, b, c (Å)			6,4890		
	α, β, γ (°)			90,0000		
	Volume of the cell (10^6 pm^3)			273,23		
	Peak	*h*	*k*	*l*	d [A]	2Theta[deg]	I [%]
	1	1	1	1	3,75100	23,701	100,0
	2	2	2	0	2,29400	39,241	83,0
	3	3	1	1	1,95600	46,384	53,0
	4	4	0	0	1,62200	56,707	12,0
Tin	Reference code[100]			00-004-0673		

β-Sn	Space group number				141		
(green	Space group				I41/amd		
references)	Crystal system				Tetragonal		
	a, b, (Å)	5,8310			c (Å)	3,1820	
	α, β, γ (°)				90,0000		
	Volume of the cell (10^6 pm^3)				108,19		
	Peak	*h*	*k*	*l*	d [A]	2Theta[deg]	I [%]
	1	2	0	0	2,91500	30,645	100,0
	2	1	0	1	2,79300	32,019	90,0
	3	2	2	0	2,06200	43,872	34,0
	4	2	1	1	2,01700	44,903	74,0
	5	3	0	1	1,65900	55,332	17,0

3.2. GERMANIUM NANOSTRUCTURES SYNTHESIZED IN THE PRESENCE OF TIN (II) BIS(BISTRIMETHYLSILYL)AMIDE

In order to fulfil the SLS mechanism tin catalyst seeds are taken, i.e. the tin (II) bis(bistrimethylsilyl)amide precursor is introduced in the reaction mixture. During the heating process the precursor decomposes forming Sn liquid droplets, which act as the catalyst seeds during the decomposition of the germanium precursor. PVP-HDE is added to the solution in order to stabilize Sn seeds and keep them from the agglomeration. The molar ratio of Ge to Sn in the solution is 2 to 1. This experiment is also performed at different temperatures such as 200 °C, 220 °C and 240 °C but the reaction time is kept the same, i.e. 30 minutes. In Figure 12 one can observe the numeric size distribution of these samples.
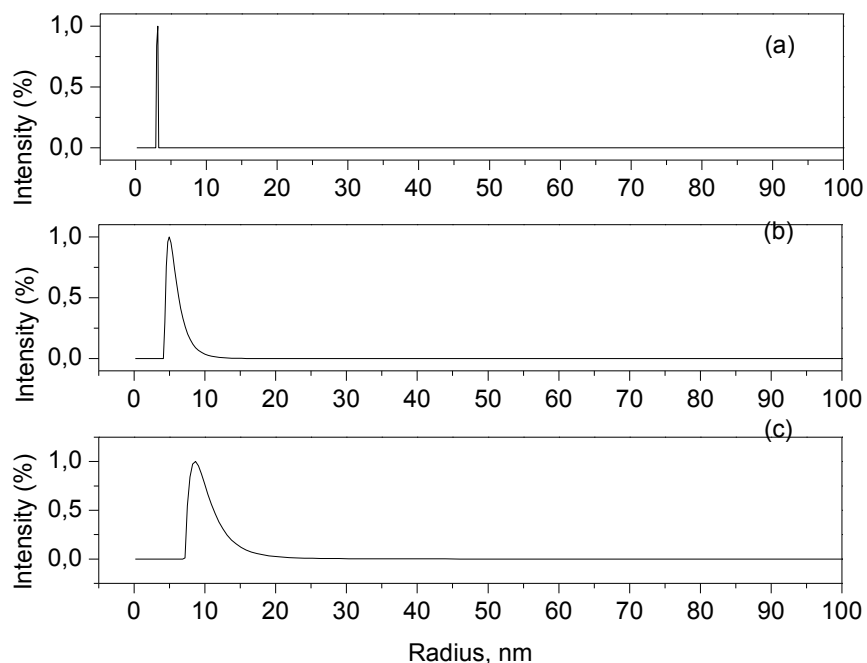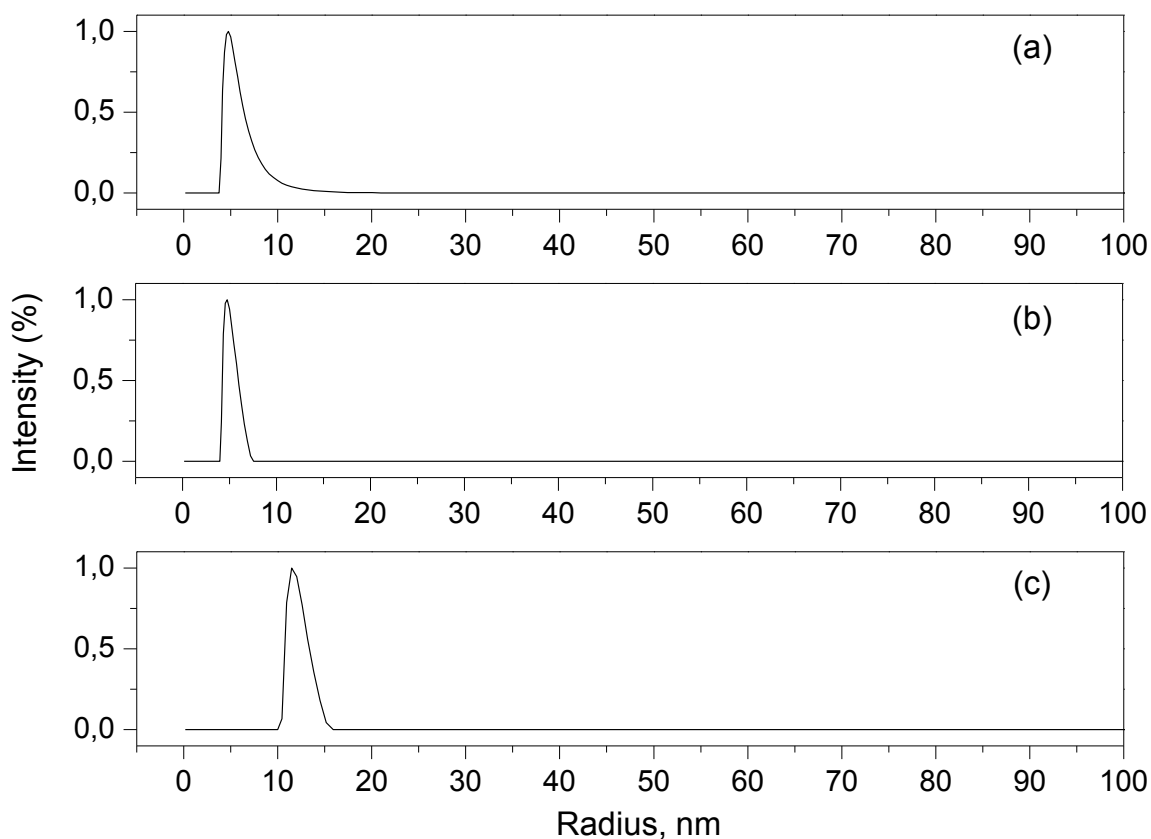
Figure 12: DLS measurements of germanium nanoparticles synthesized in the presence of Sn(HMDS)$_2$ precursor: (a) at 200 ^{o}C for 30 minutes; (b) at 220 ^{o}C for 30 minutes; (c) at 240 ^{o}C for 30 minutes.

The average diameter of the particles grown at 200 ^{o}C is 6.12 ± 0.04 nm (Figure 12a). The numeric distribution of the Ge nanoparticles grown at 220 ^{o}C and 240 ^{o}C are 11.2 ± 0.4 nm and 19.8 ± 0.4 nm respectively (Figures 12b and 12c). In this case one can also observe that with increasing temperature the size of nanoparticles becomes bigger.
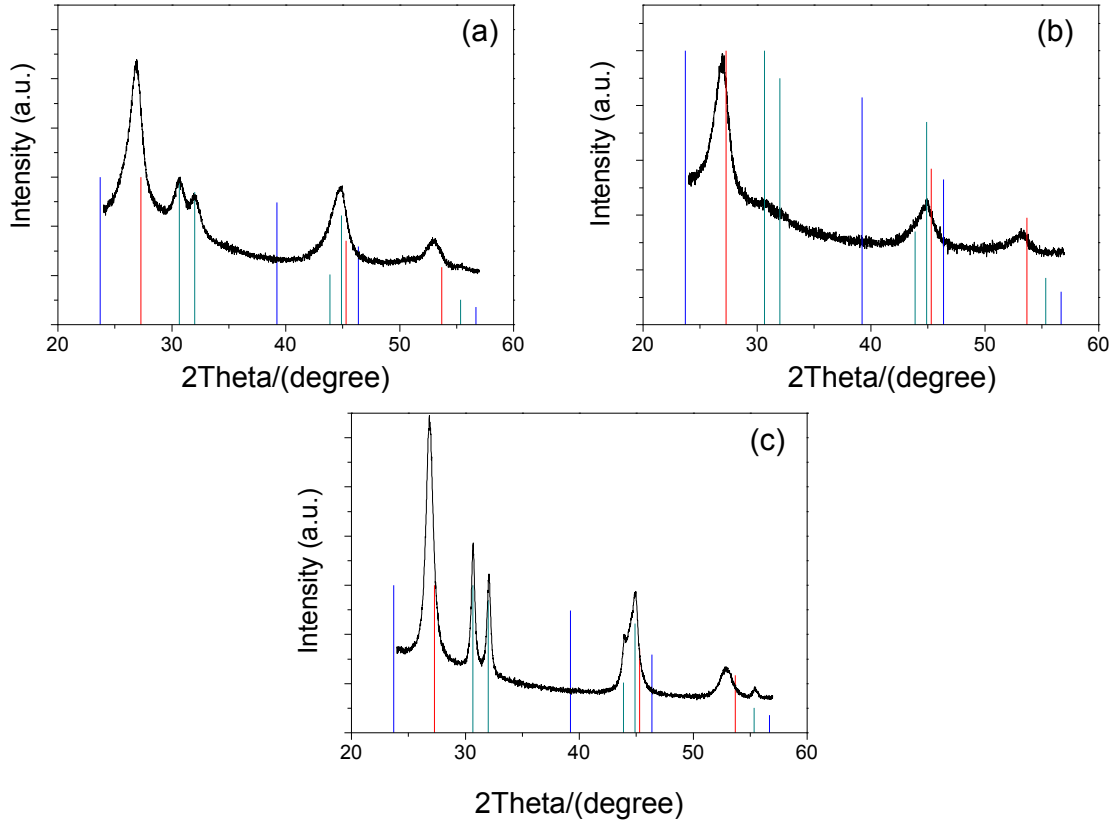
Figure 13: XRD patterns of germanium nanoparticles synthesized in the presence of Sn(HMDS)$_2$ precursor: (a) at 200 °C for 30 minutes; (b) at 220 °C for 30 minutes; (c) at 240 °C for 30 minutes (References: α-Sn 00-005-0390 – blue, β-Sn 00-004-0673 – green, Ge 00-004-0545 – red).

In Figure 13 the XRD patterns of the obtained Ge nanostructures are shown. All three diffractograms demonstrate the presence of crystalline structure. Red references represent the Ge reflexes; the green ones show β-Sn (tetragonal) crystallographic structure and the blue reflexes represent the α-Sn cubic structure. The detailed information about the crystallographic structure of both elements is shown in Table 1. As one can see from the XRD patterns the peaks, which correspond to germanium, are slightly displaced towards

lower Bragg's angles, which means that the primitive unit cell has become bigger. The unit cell becomes larger when there are bigger foreign atoms are incorporated, in this case Sn atoms. This fact brings us to the conclusion that some tin is incorporated in the Ge lattice during the synthesis process. As far as tin is concerned, one can notice only the presence of the tetragonal phase, because the cubic phase (α-Sn) is only stable below 13.2 ^{o}C. The measurements are taken at room temperature.

Once germanium crystalline structures are obtained via the microwave reactor the molar ratio between germanium and the tin precursor is increased in order to synthesize more elongated nanostructures. The molar ratio of Sn(HMDS)$_2$ and Ge(HMDS)$_2$ precursors varies from 1 to 5 and 1 to 7 to 1 : 11. All three reactions are performed in the same conditions and the reaction is carried out at 200 ^{o}C for 30 minutes as both the temperature and the reaction time appear to be optimal for decomposition of both precursors and for growing crystalline Ge nanostructures. In Figure 14 the numeric size distribution of the obtained nanostructures is shown. The structures obtained at 200 ^{o}C that have molar ratio of Sn to Ge 1 to 5 are 11.2 ± 0.5 nm in diameter, while the ones that have molar ratio 1 : 7 and 1 : 11 are 10.2 ± 0.3 nm and 24.4 ± 0.2 nm respectively. As we can conclude from DLS measurements the obtained structures are slightly bigger than the ones grown at 200 ^{o}C with precursors molar ratio 1 : 2, but they are about the same size with the ones, that are grown at 220 ^{o}C and 240 ^{o}C with precursors molar ratio 1 : 2.

Figure 14: DLS measurements of germanium nanoparticles synthesized in the presence of Sn(HMDS)$_2$ precursor at 200 °C for 30 minutes with molar ratio of Sn to Ge: (a) 1 : 5; (b) 1 : 7; (c) 1 : 11.

The XRD patterns in Figure 15 show the presence of crystalline structure only in the case of 1 to 5 precursors' molar ratio. As in previous experiments the Ge reference reflexes are misplaced slightly to the left and there is no sign of the cubic tin phase. In all three diffractograms one can observe the presence of reflexes at ca. 21.7° and 22.5° which does not correspond with neither tin nor germanium references. This can point on the presence of some unknown synthesis by-products, which are not washed away properly during the purification step.
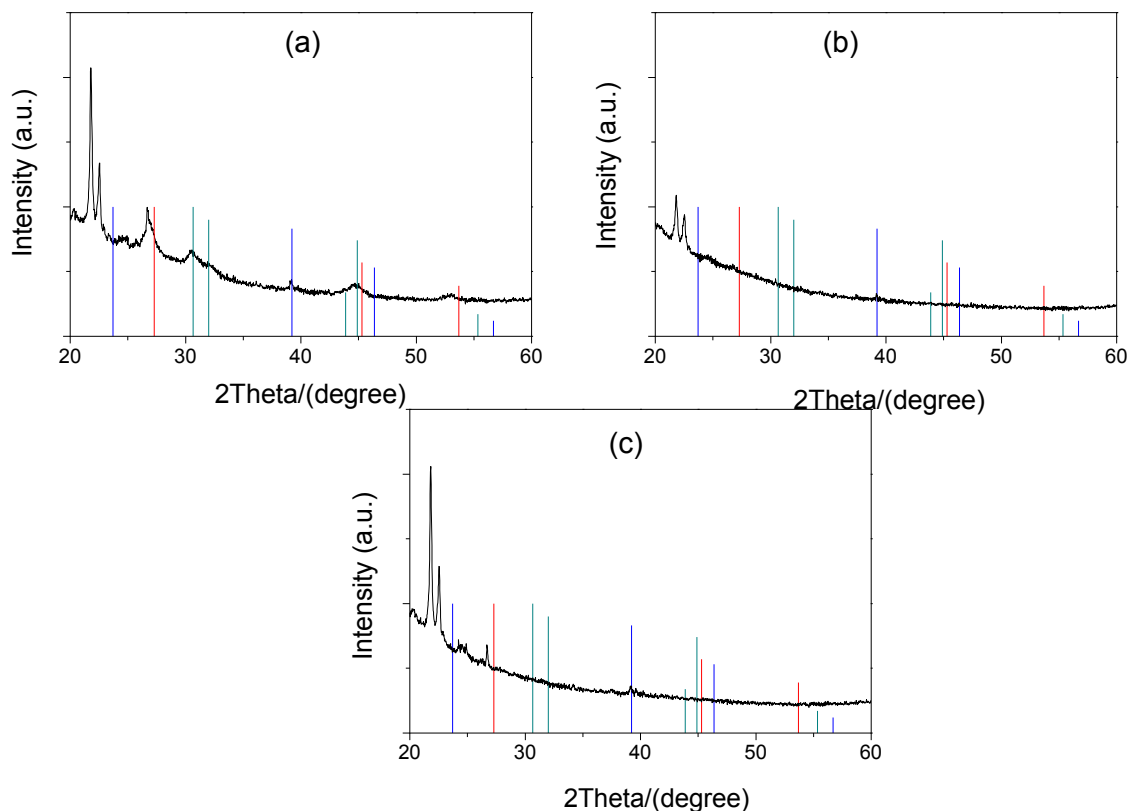
Figure 15: XRD patterns of germanium nanoparticles synthesized in the presence of Sn(HMDS)$_2$ precursor at 200 °C for 30 minutes with molar ratio of Sn to Ge: (a) 1 : 5; (b) 1 : 7; (c) 1 : 11 (References: α-Sn 00-005-0390 – blue, β-Sn 00-004-0673 – green, Ge 00-004-0545 – red).

The TEM images in Figure 16 illustrate the obtained germanium nanostructures in presence of Sn(HMDS)$_2$ with molar ratio of both elements 2 to 1 (Ge : Sn). One can notice the nanostructures from about 25 to 50 nm in length and from 5 to 25 nm in diameter. The Z-contrast illustrates that the darker seed belongs to tin and the lighter tail to germanium. The shape of the particles terminating the elongated structures is close to hemispherical. It is also noticeable that in some structures Sn atoms are present not only on the seed but also in the body of the structure.
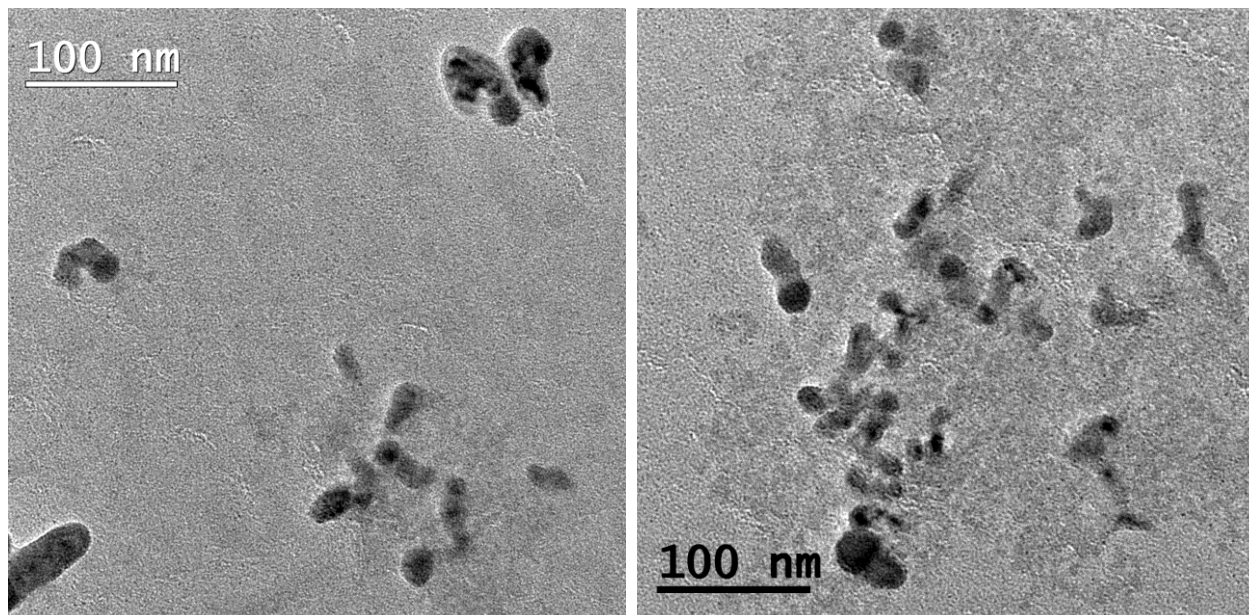
Figure 16: TEM images of Ge nanostructures made with molar ratio 2 to 1 (Ge : Sn).

The TEM images in Figure 17 show the obtained nanostructures more closely. The bent structure is approximately 60 nm in length and 12 nm in diameter. The HR-TEM image illustrates a close up of this structure. The parallel position of the planes brings one to the conclusion that we deal with single crystal structure. The fast Fourier transformation (FFT) image reveals some dots that help to index the crystallographic planes (Figure 17 below). By the calculated distance in the lattice one can conclude that the two dots on the image correspond to Ge (111) and Ge (110) planes. The distance in the primitive cell calculated from the image equals 3.27 nm while the theoretical one is 3.26 nm (reference PDF 04-0545).
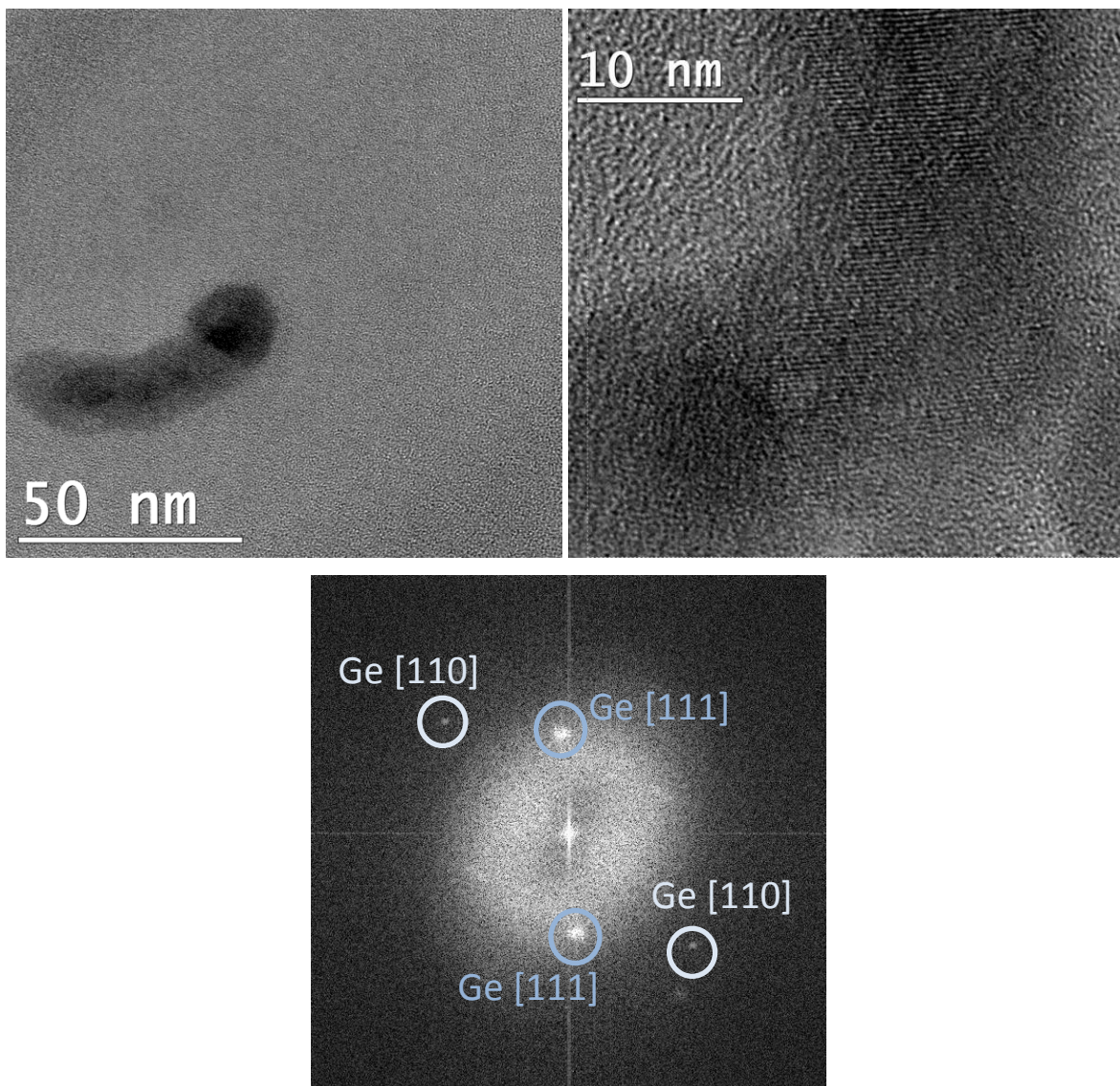
Figure 17: TEM images and FFT of Ge nanostructures made with molar ratio 2 to 1 (Ge : Sn).

The HR-TEM in Figure 18 illustrates another crystalline structure in this sample. One can still notice the single crystal structure, which contains a hemispherical seed and an elongated tail. The FFT image shows the presence of Ge (111) and Sn (101) planes (references PDF 04-0545 and PDF 04-0673 respectively). The distance calculated with the interface for Sn (101) plane equals to 2.83 nm while the theoretical ones is 2.79 nm.
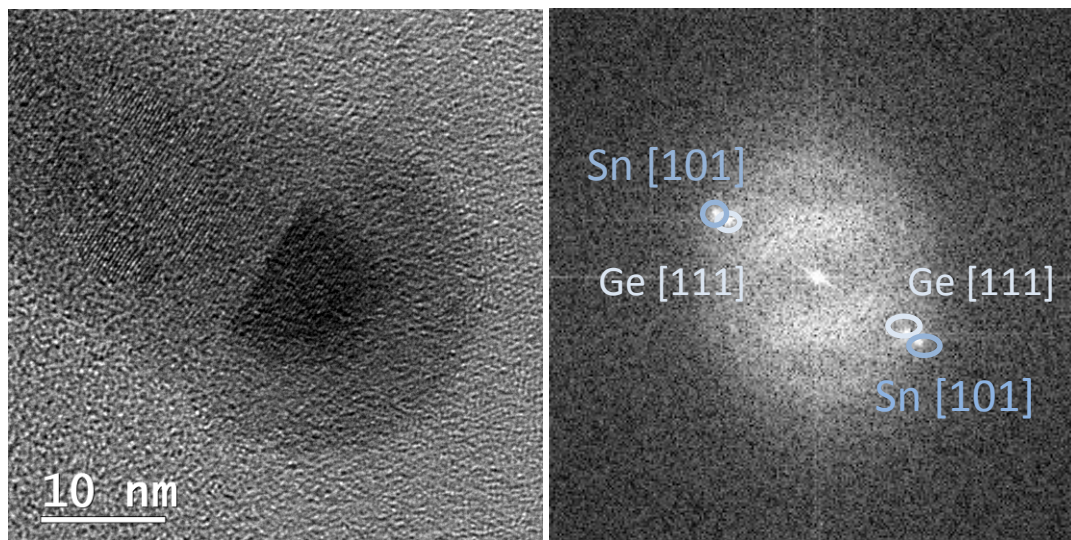
Figure 18: TEM image and FFT of Ge nanostructures made with molar ratio 2 to 1 (Ge : Sn).

In Figure 19 SEM images illustrate the structure of the obtained germanium nanostructures while the molar ratio between two precursors is 5 to 1 (Ge : Sn). In the first two images one can only see the organic matrix, but as the resolution is increased one can notice some metallic seeds embedded into the organic matrix. The diameter of these seeds is approx. 15 nm, the size distribution of the nanoparticles in the image appear to be homogeneous. These images show the presence of the excessive quantities of the organic substance in the sample, signifying a need for improvement in the purification procedure.
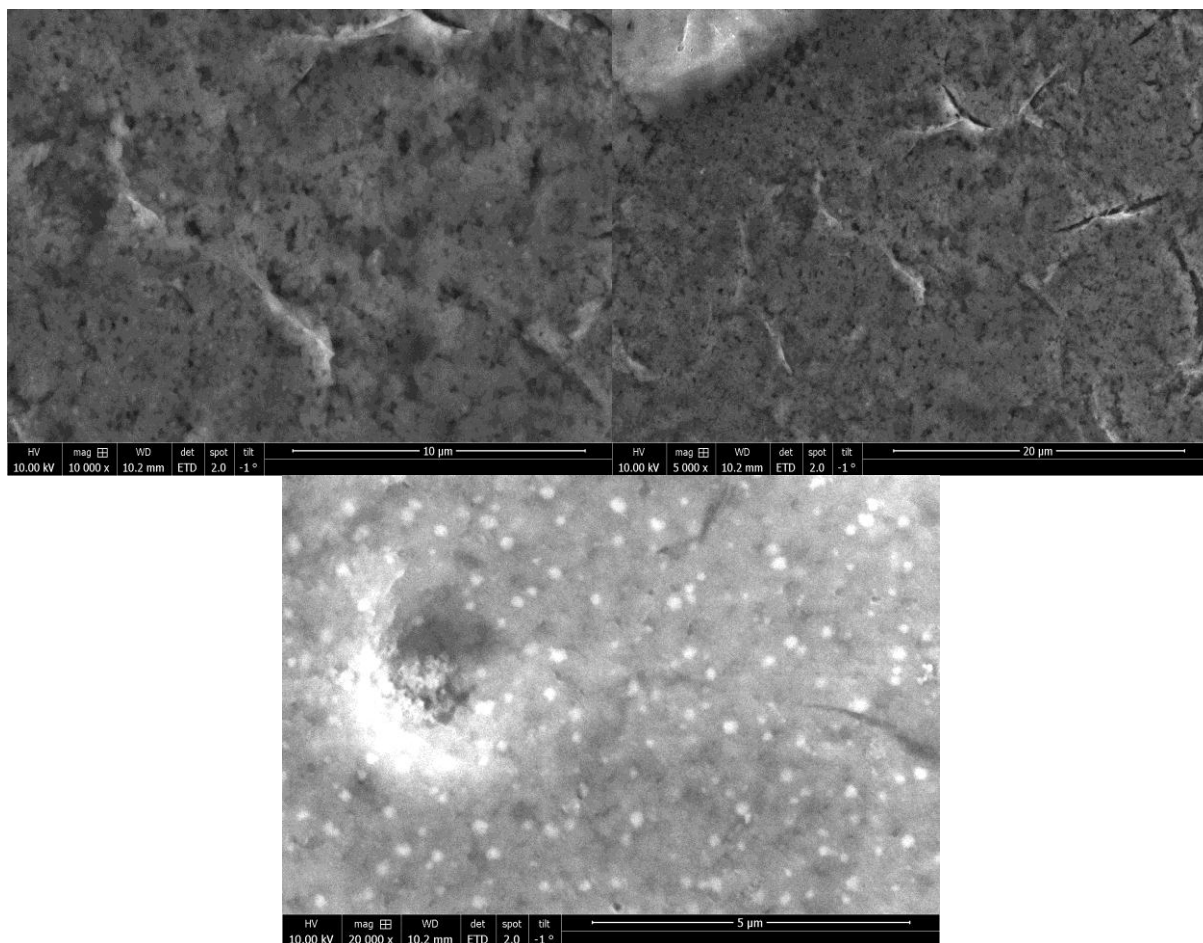
Figure 19: SEM images of Ge nanostructures made with molar ratio 5 to 1 (Ge : Sn).

In order to increase the aspect ratio of the Ge nanostructures another strategy was chosen. The reaction was performed in two steps, where at the beginning only half of the total amount of Ge(HMDS)$_2$ was added to the reaction mixture and the reaction ran for 30 minutes at 200 °C before being cooled to room temperature. Then the second half of Ge(HMDS)$_2$ was added to the solution and the reaction was heated up to 200 °C for another 30 minutes. The total molar ratio of Sn(HMDS)$_2$ to Ge(HMDS)$_2$ is equal to 1 : 6.3. In Figure 20 one can observe the DLS and XRD measurements of the resulting nanostructures.
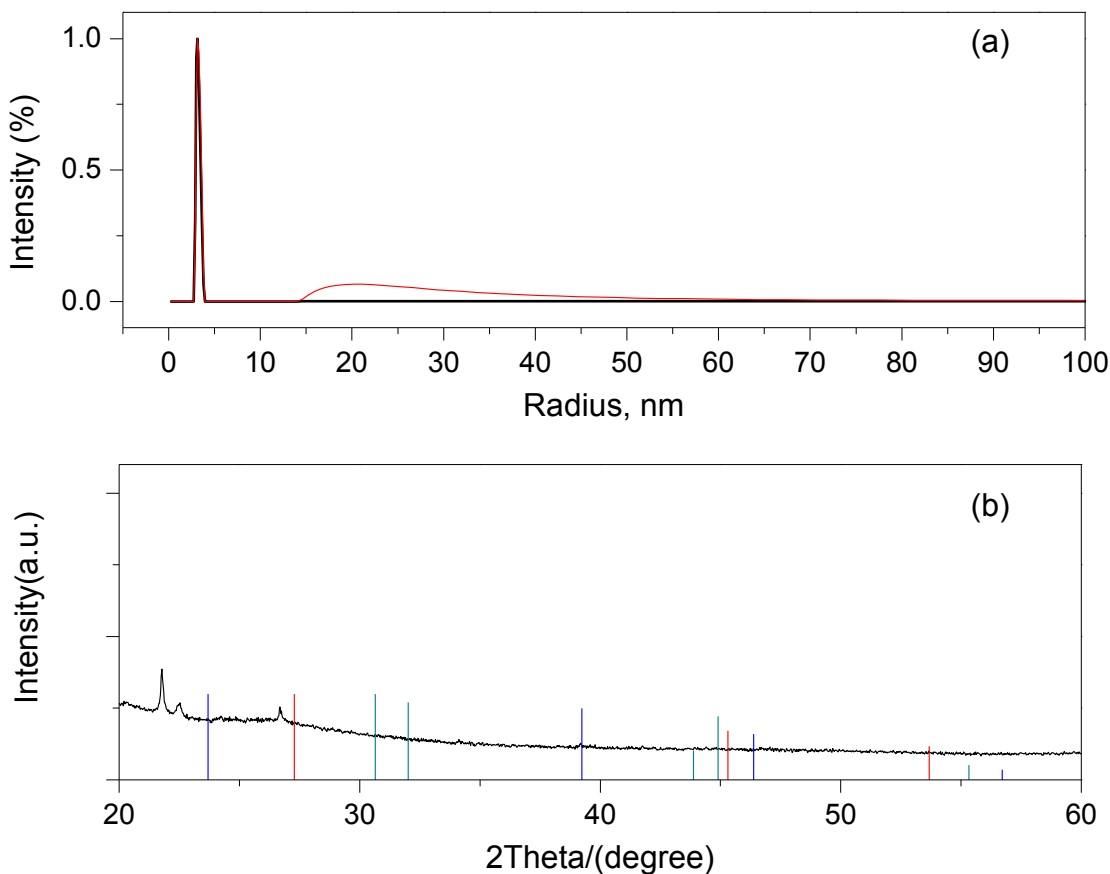
Figure 20: DLS size distribution (numeric – black, mass – red) (a) and XRD pattern (References: α-Sn 00-005-0390 – blue, β-Sn 00-004-0673 – green, Ge 00-004-0545 – red) (b) of Ge nanostructures synthesized in two steps at 200 °C for 1 hour (molar ratio of Sn to Ge 1 : 6.3).

The black curve in Figure 20a represents the numeric size distribution while the red represents the mass size distribution. As both curves show the main particle size is equal to 6.5 ± 0.1 nm, although the mass size distribution demonstrates the presence of bigger structures about 64.8 ± 1.4 nm in diameter. The XRD pattern of the obtained structures (Figure 20b) shows no sign of the crystalline Ge structure in the sample besides the organic impurities.

The crystalline germanium nanostructures are obtained using tin as metallic catalyst seed in order to perform the SLS mechanism. Although, as the molar ratio of the precursors decreases the crystallinity of the structures decreases as well. Thus the structures with molar ratio Sn : Ge is 1 to 5 only slight reflexes can be observed with respect to definite reflexes of the sample with molar ratio Sn : Ge 1 to 2. Starting from the two-step reaction with molar ratio 1 to 6.3 and the sample with molar ratio 1 to 7 there are no further reflexes of either Ge or of Sn observed.

3.3. THERMAL DECOMPOSTION OF DIPHENYLGERMANE

As an alternative precursor for germanium nanostructures synthesis diphenylgermane is taken, diphenylgermane decomposes in the microwave reactor at 240 ^{o}C in the presence of Sn(HMDS)$_2$, which is used to form Sn catalyst seeds. The synthesis procedure is similar to the ones used in previous chapters. In Figure 21a one can observe the numeric size distribution of the obtained nanoparticles. The diameter equals 19.8 ± 0.3 nm. From the XRD pattern in Figure 21b one can notice strong and very definite reflexes of tetragonal Sn and very weak ones from the cubic Sn. The Ge reflexes are also present and they are misplaced towards the lower Bragg's angle, which as in previous cases speaks of the formation of a solid solution with introduction of Sn atoms into the crystal lattice.
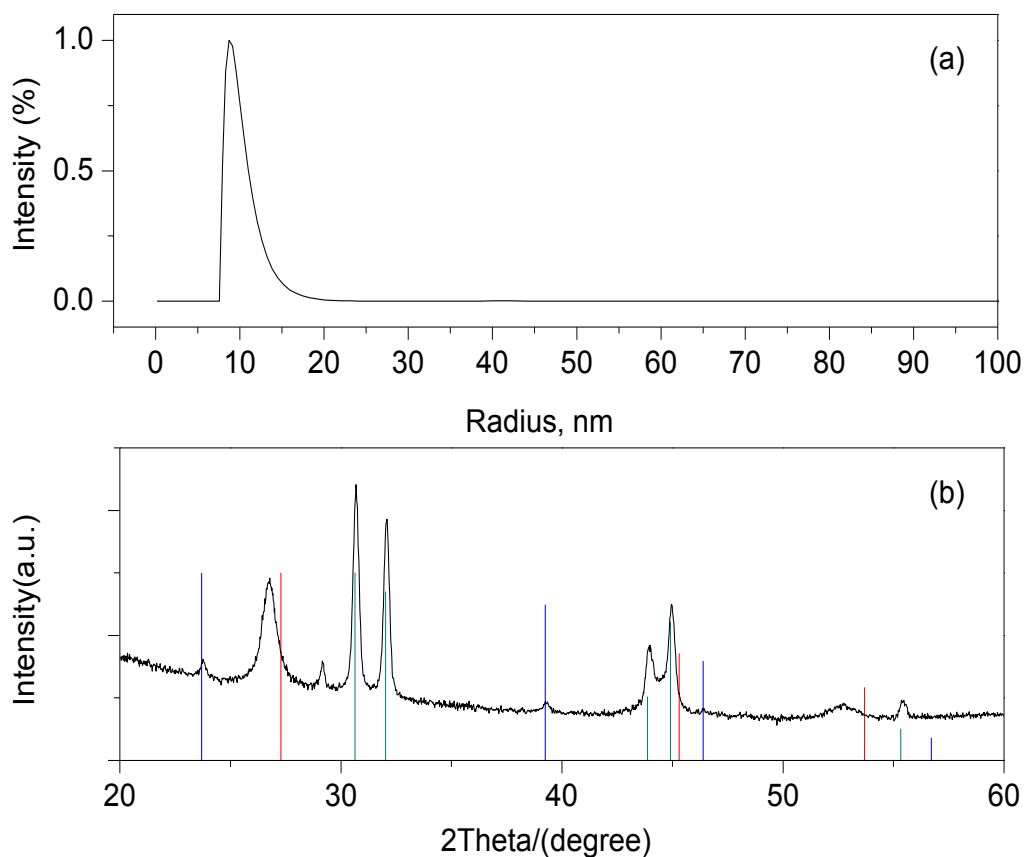
Figure 21: DLS measurement (a) and XRD pattern (b) of germanium nanostructures obtained by thermal decomposition of diphenylgermane in the presence of Sn(HMDS)$_2$ at 240 °C for 30 minutes (References: α-Sn 00-005-0390 – blue, β-Sn 00-004-0673 – green, Ge 00-004-0545 – red).

In Figure 22 SEM images illustrate the obtained structure. There are areas, where single nanoparticles can be observed (Figure 22 right), which brings us to the conclusion that the bigger agglomerates shown in this image consist of smaller nanoparticles.
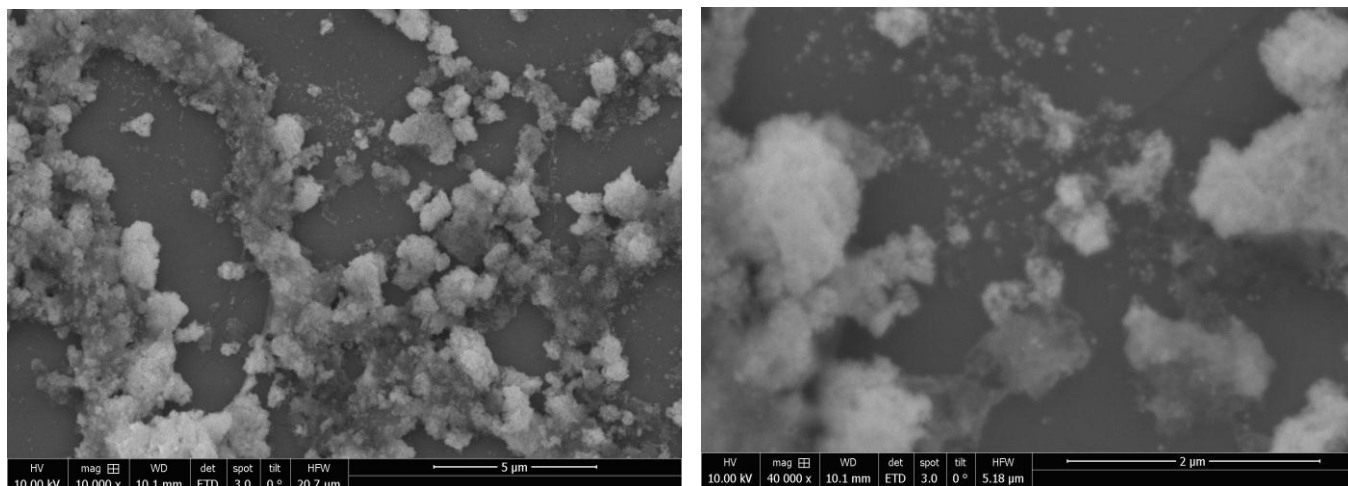
Figure 22: SEM images of germanium nanostructures obtained by decomposition of diphenylgermane.

3.4. GERMANIUM NANOSTRUCTURES SYNTHESIZED IN THE PRESENCE OF TIN NANOPARTICLES

In order to optimize the growth process, pre-synthesized Sn nanoparticles were target. The synthesis procedure of the Sn nanoparticles is described in section 5.5.1. The quantity of Sn nanoparticles taken corresponds to the molar ratio between Ge and Sn 5 to 1. The synthesis procedure remains similar to the previous ones. The reaction is carried out at 240 ^{o}C for 30 minutes. The purification step is carried out for one part with dry methanol and the second part with dry ethanol. In Figure 23 one can see the DLS numeric and mass size distribution of the both parts. According to the numeric size distribution the nanostructures purified with ethanol are 28.2 ± 0.2 nm in diameter and the ones purified with methanol are 77.8 ± 0.6 nm. The mass size distribution of the structures purified with ethanol shows two wider peaks where ca. 31.1 % of the total amount of the nanostructures is 28.2 ± 0.2 nm in diameter and 68.9 % is 433.2 ± 1.4 nm. The mass size distribution of the methanol-purified Ge structures demonstrates the diameter of 189.2 ± 1.6 nm. The formation of such big

structures can be explained by the fact that tin nanoparticles solution used for the synthesis still contained some alcohol remained from its purification procedure. The alcohol reacts with the Ge precursor forming alkoxides. The alkoxide groups, in their turn, form much stronger bonds with germanium and the decomposition is only possible at higher temperatures.
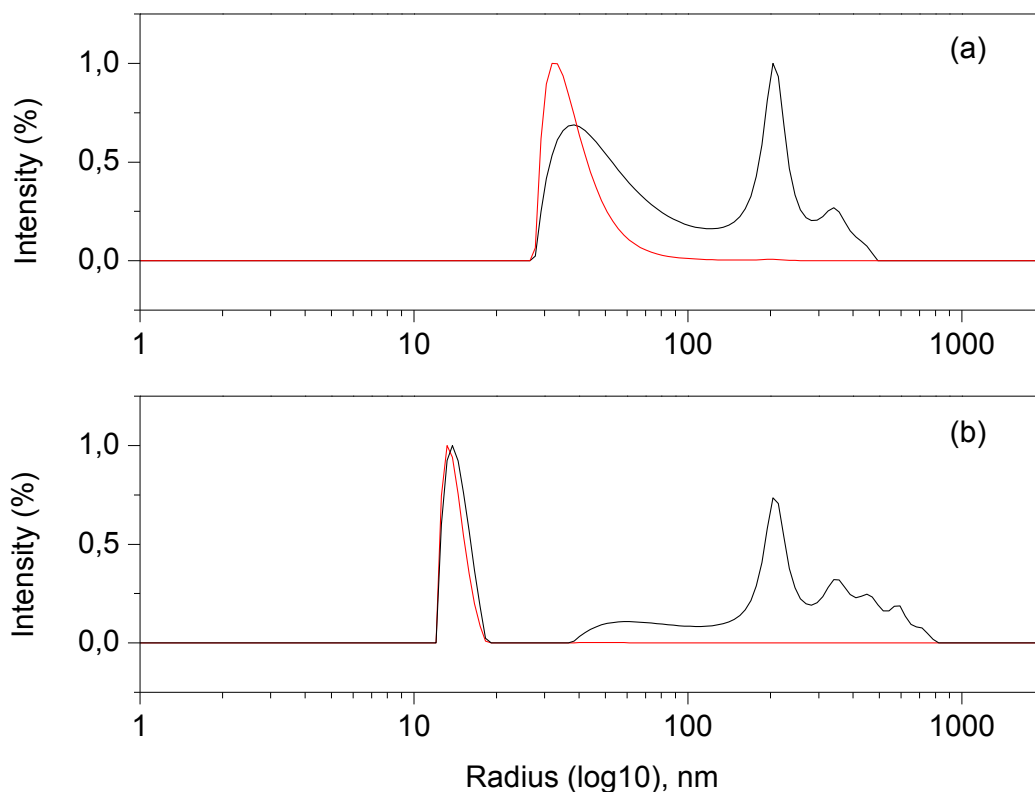

Figure 23: DLS measurements of the nanostructures obtained in presence of Sn nanoparticles (a) purified with methanol (b) purified with ethanol (red – numeric size distribution, black – mass size distribution).

One can notice that the germanium particles purified with ethanol are smaller independently from the calculation mode. Presumably the monomer structures are more stable in ethanol and the agglomeration into bigger structures such as dimers makes them more stable in methanol. One can notice it from the position of the first peak of each curve.

The second peak of the mass size distribution curve is situated at the same position in both graphics, which points on the formation of bigger stable agglomerates in the solution.

The XRD pattern in Figure 24 shows that the obtained structures in both cases are amorphous.
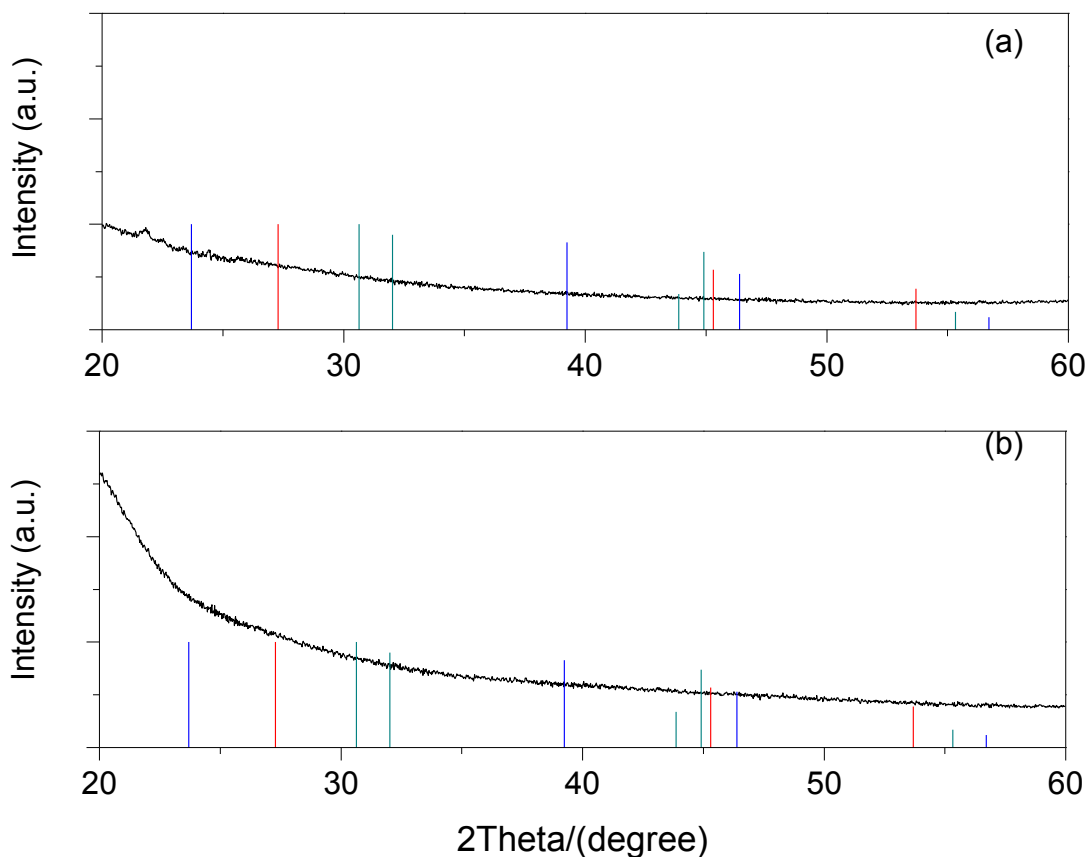
Figure 24: XRD patterns of germanium nanoparticles synthesized in the presence of Sn nanoparticles purified with: (a) ethanol, (b) methanol (References: α-Sn 00-005-0390 – blue, β-Sn 00-004-0673 – green, Ge 00-004-0545 – red).

The same synthesis is also carried out using diphenylgermane as a precursor in the presence of Sn nanoparticles, but no decomposition took place, even at 260 °C. The characterization of the synthesized Sn nanoparticles is described fully in the section 3.5.

Namely the TGA investigations (Figure 26) show the molar ratio between PVP-HDE copolymer and Sn, which equals 5.6 to 1 (PVP-HDE : Sn), while molar ratio in the previous synthesis where $Sn(HMDS)_2$ is used this ratio varies from 10.9 : 1 to 18.4 : 1 (PVP-HDE : Sn). Large amounts of polymer does not allow for the performance of the SLS growth mechanism which is why the obtained structures are amorphous.

3.5. TIN NANOPARTICLES CHARACTERIZATION

The aim of this part of the work is to synthesize less than 10 nm uniform tin nanoparticles with narrow size distribution in order to use them for the synthesis of Ge nanostructures. The first synthetic route is developed by Buhro *et al.*[40] and adapted for Sn nanoparticles by Lu *et al.*[41] The whole stepwise synthesis procedure is described in section 5.5.1. The purified nanoparticles capped with PVP-HDE copolymer are dissolved in toluene. In Figure 25b the numeric size distribution determined by DLS technique is shown. The obtained nanoparticles have narrow size distribution (1.9 %) and are 10.4 ± 0.2 nm in diameter. The XRD pattern in Figure 25a shows the amorphous structure of the obtained nanoparticles. It can be explained with the high concentration of the polymer in the sample, which shields the nanoparticles, and weakens the signal coming from the particles drastically. It also brings us to the conclusion that DLS signal could come mainly from the polymer.

In order to determine the amount of polymer in the solution and its molar ratio with respect to tin TGA tests are performed. The TGA test is performed two times in the Al_2O_3 crucible so the more precise results can be obtained. The sample is heated to 600 °C with 5 °C/min heating rate. In Figure 26 one can observe the weight loss in % due to the chemical and physical processes as a function of the temperature represented in the TGA diagram. The weight loss in the first step has an onset temperature of ca. 127.3 °C and equals 35.73 mass.%. It corresponds to a partial amount of toluene in the solution. The weight loss in the

second step happens at ca. 416.1 °C and it is equal to 57.55 mass.%. This weight loss corresponds to the total amount of the polymer in the solution. The residual is present in form of SnO_2 and its mass equals 6.86 mass.%. From this data one can calculate the concentration of Sn nanoparticles in the solution and the molar ratio between the capping agent and Sn. The concentration of Sn nanoparticles dissolved in toluene equals 0.03905 mol/L. The molar ratio between PVP-HDE copolymer and Sn is 1 to 5.6. As was already written in the previous chapter, the quantity of the polymer in the solution exceeds the amount of polymer used for the synthesis approx. three times.
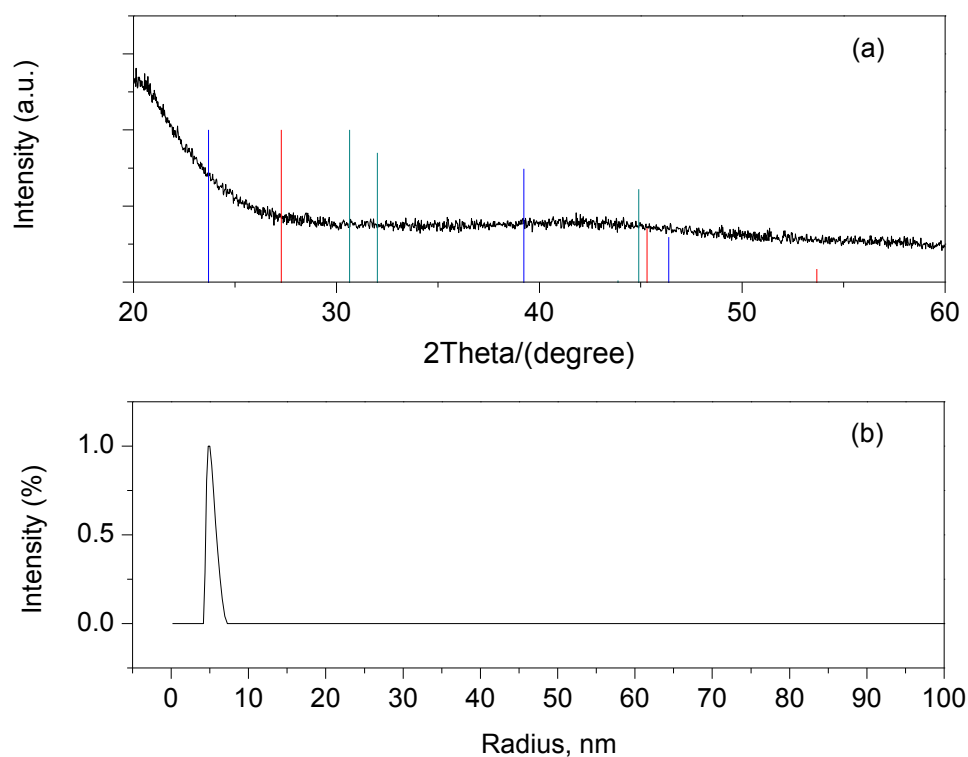
Figure 25: XRD pattern (a) and DLS measurement (b) of tin nanoparticles capped with PVP-HDE copolymer (References: α-Sn 00-005-0390 – blue, β-Sn 00-004-0673 – green, Ge 00-004-0545 – red).
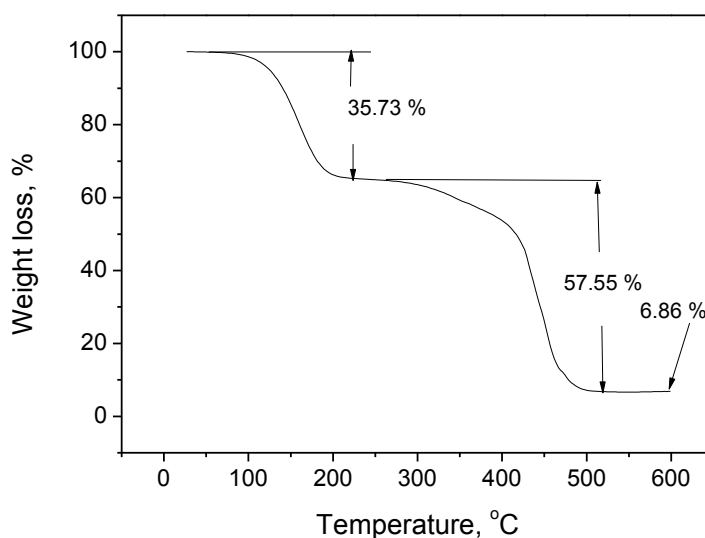
Figure 26: TGA diagram of Sn nanoparticles capped with PVP-HDE copolymer.

There was an attempt to reduce the amount of polymer by washing the nanoparticles more times, but with further washing the nanoparticles aggregated and could not be re-dispersed again. The PVP-HDE copolymer appears to be a strong capping agent, because the nanoparticles remained stable even in the air conditions; however it is difficult to use Sn nanoparticles for the further synthesis.

As the germanium nanostructures obtained using Sn nanoparticles capped with PVP-HDE copolymer were amorphous, new routes of the synthesis of Sn nanoparticles were investigated. For instance, Watanabe *et al.*[44] reported a thermal reduction method, which is fully described in the section 5.5.3. The colour of the obtained nanoparticles is gray. From the colour one can approximately estimate the size of the obtained particles, due to the nanostructures' optical properties. Sn nanoparticles in the nano range have brownish-gray colour, while the ones obtained by Watanabe route differs from it. The DLS investigation in Figure 27 confirms the formation of the bigger particles. The average diameter according to the numeric size distribution of 63.0 % of all particles is 100.6 ± 0.2 nm while the 37.0 % of the particles have diameter, which is equal to 553.8 ± 1.0 nm. As far as the mass distribution

is concerned there is only one main peak and the diameter of the particles is 1925.5 ± 1.4 nm.
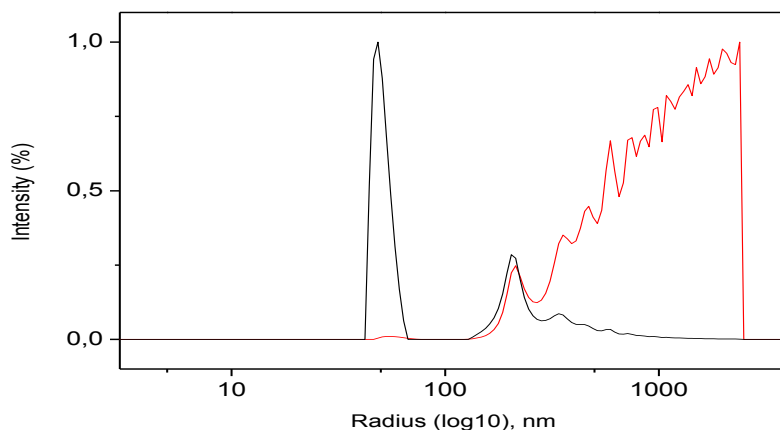
Figure 27: DLS test of tin nanoparticles capped with oleylamine (black – numeric size distribution, red – mass size distribution).

Another possibility to synthesize Sn nanoparticles is to use $Sn(HMDS)_2$ and perform the synthesis in the microwave reactor. The synthetic route is fully described in the section 5.5.4. The obtained nanoparticles are capped with dodecylamine, so the surface stabilizer is changed to the oleic acid. In Figure 28 the DLS and XRD studies are shown. The diameter of nanoparticles equals 3.80 ± 0.08 nm, while the size distribution is 2.1 %. On the XRD pattern one can see weak reflexes of the tetragonal Sn. Their low intensity can be explained with the small particles' size.
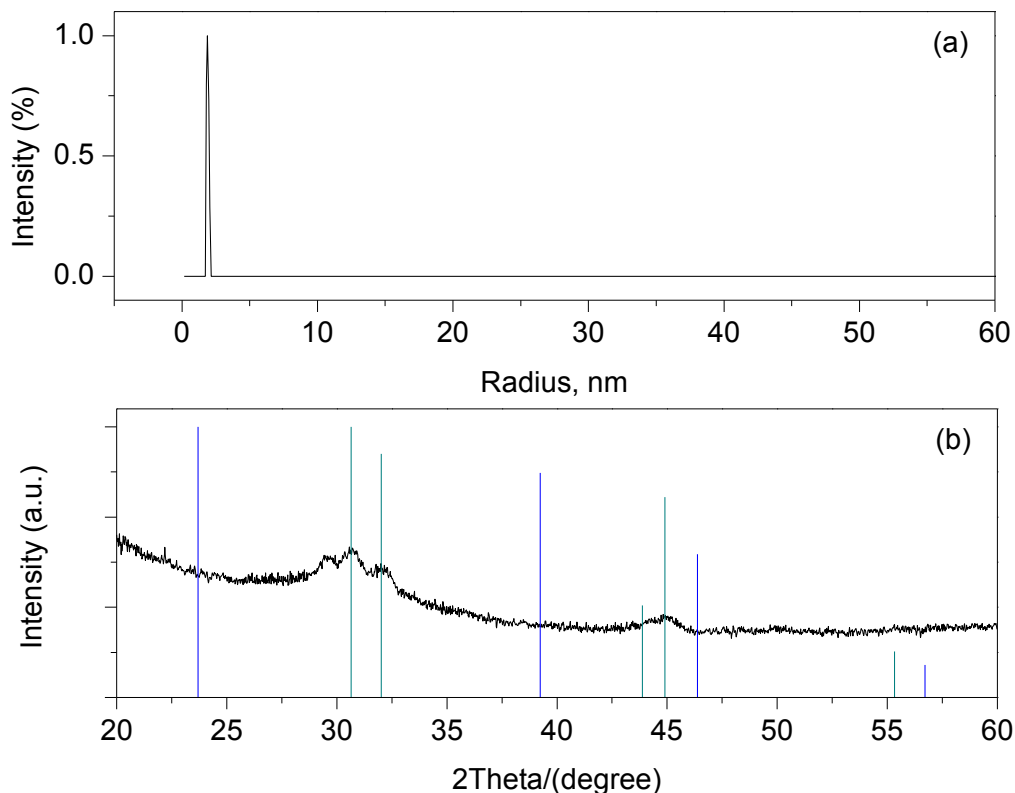
Figure 28: DLS measurement (a) and XRD pattern (b) of tin nanoparticles capped with oleic acid and obtained in the microwave reactor (References: α-Sn 00-005-0390 – blue, β-Sn 00-004-0673 – green).

Since the tin nanoparticles capped with the polymer are not suitable for Ge nanostructure synthesis there is another important synthetic route for Sn nanoparticles formation reported by Kravchyk and co-workers,[42] which is described fully in the section 5.5.2. The reaction time is varied from 10 seconds to 1 hour according to the instructions in the article. The obtained nanoparticles are capped with oleic acid. In Figure 29 the DLS measurements of the tin nanoparticles obtained during one hour and 10 seconds reactions are shown. The particles obtained during 1 hour reaction are 57.4 ± 0.4 nm and the ones obtained after 10 seconds reaction are 11.4 ± 0.1 nm. In Figure 30 one can observe the XRD patterns of the obtained nanoparticles. The presence of the tetragonal tin phase is observed

in both cases; the reflexes from the particles obtained after 1 hour are stronger, because the particles are bigger and hence the crystallites size is bigger.
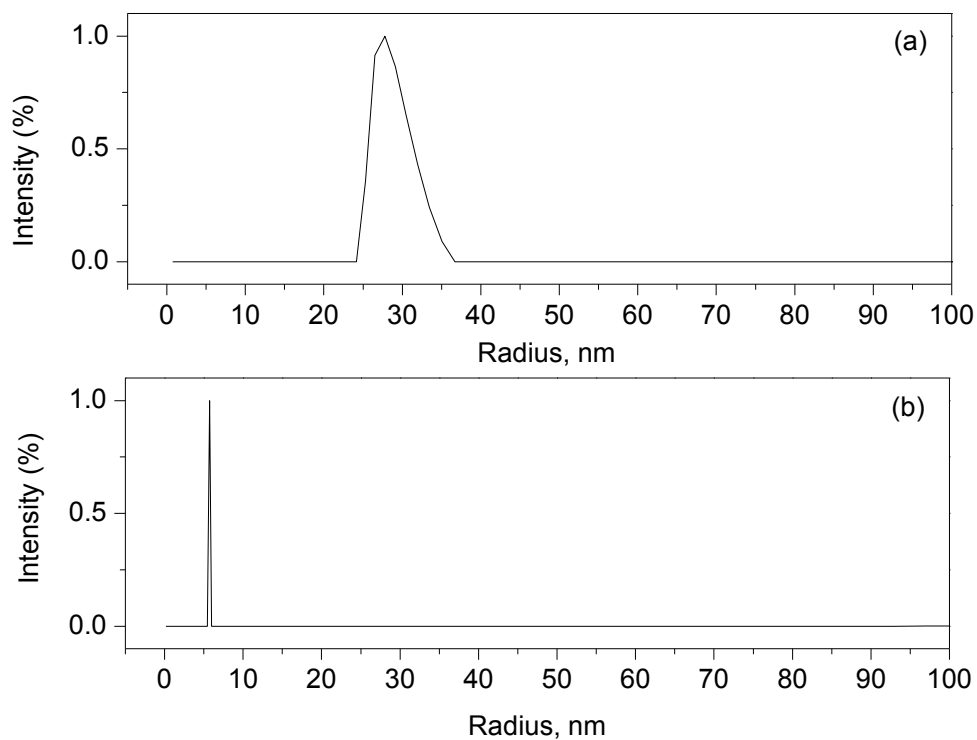

Figure 29: DLS measurements of the obtained tin nanoparticles capped with oleic acid (a) 1 hour reaction (b) 10 seconds reaction.
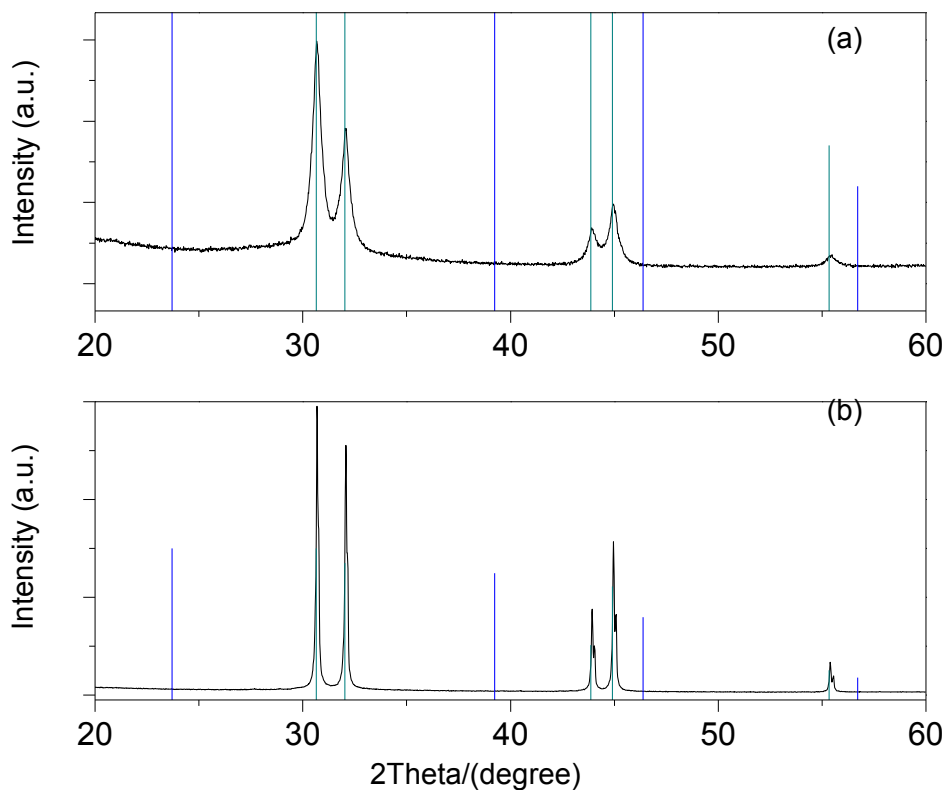
Figure 30: XRD patterns of the obtained tin nanoparticles capped with oleic acid (a) 10 seconds reaction (b) 1 hour reaction (References: α-Sn 00-005-0390 – blue, β-Sn 00-004-0673 – green).

In Figure 31 the SEM images of Sn nanostructures are shown. At the SEM images above one can see the structure that consists of the agglomerates of about 4 – 5 µm in diameter or ones that are even bigger. With the increasing resolution one can see that these agglomerates consist of nanoparticles. The pictures are taken from the 10 seconds reaction sample.
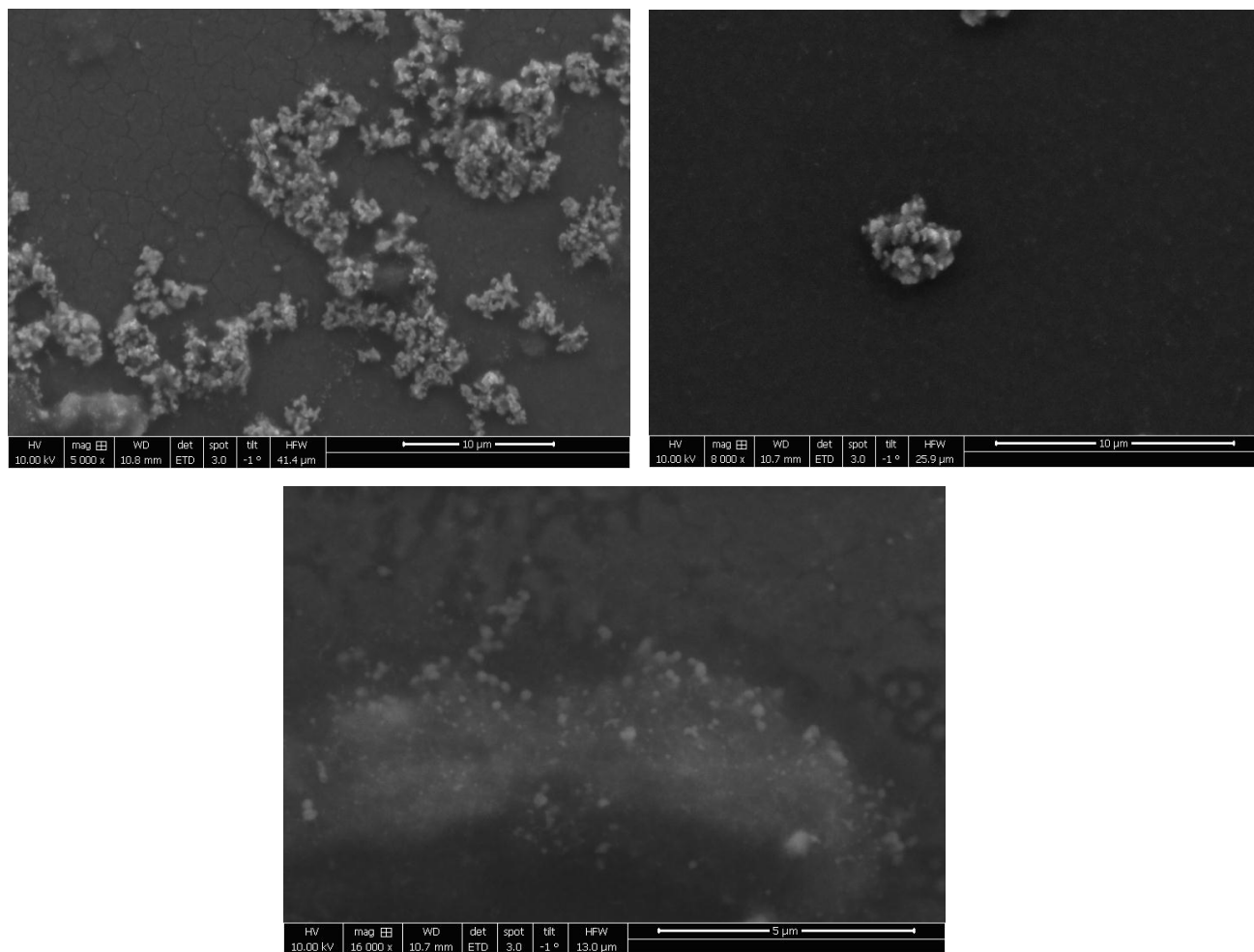
Figure 31: SEM pictures of tin nanoparticles capped with oleic acid.

These Sn nanoparticles are then used for Ge nanostructures synthesis, but the decomposition reaction does not take place, because the excess of the oleic acid remaining in the sample reacts with the precursor and destroys it. So some TGA investigations are performed in order to determine the molar ratio between Sn and oleic acid. The samples are also purified differently in order to study what way is best for washing off the oleic acid. For this purpose ethanol and n-butanol are taken in different proportions: starting from 100 % ethanol and finishing with 100 % butanol.

In order to perform the TGA measurements new samples of the nanoparticles are synthesized using the same synthetic route. In Figure 32 one can see the DLS measurements of the obtained and purified samples. The size distribution of each sample can be found in Table 2.
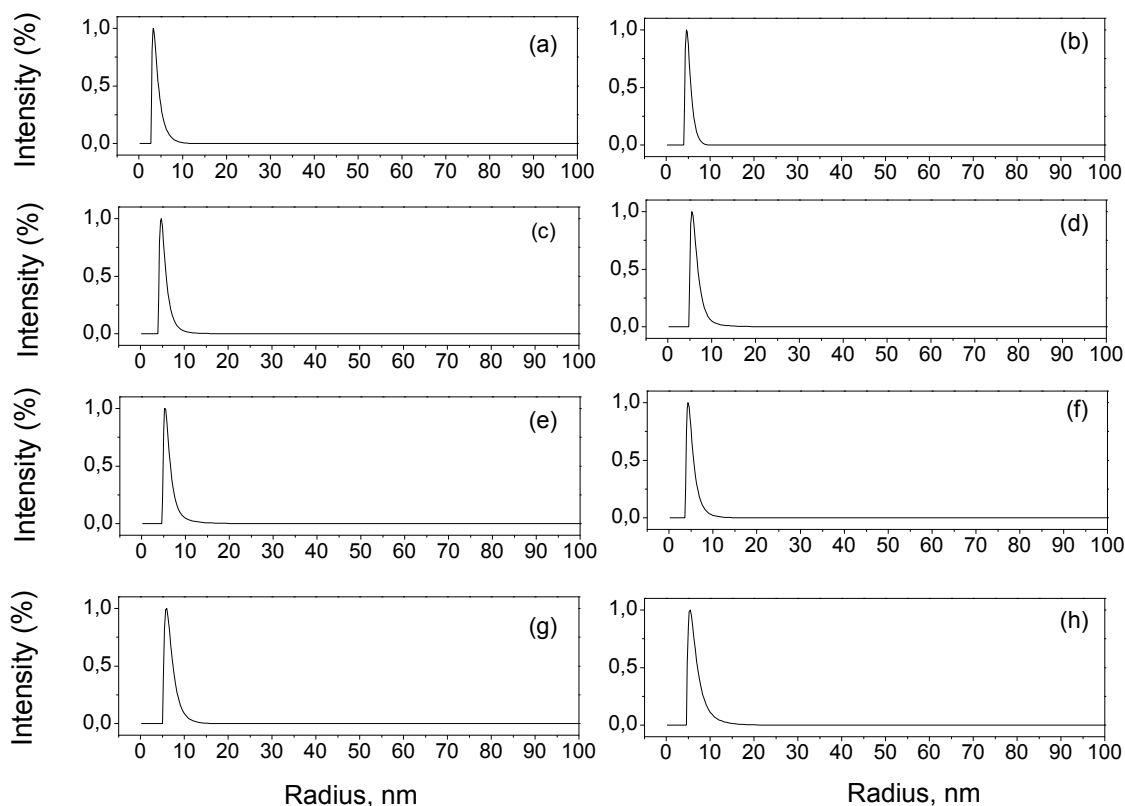
Figure 32: DLS numeric size distribution of the obtained Sn nanoparticles: (a) 1st sample after the exchange reaction with oleic acid; (b) 1st sample purified with ethanol (100 %); (c) 2nd sample after the exchange reaction with oleic acid; (d) 2nd sample purified with 80 vol.% ethanol and 20 vol.% butanol; (e) 2nd sample purified with 50 vol.% ethanol and 50 vol.% butanol; (f) 3rd sample after the exchange reaction with oleic acid; (g) 3rd sample purified with 20 vol.% ethanol and 80 vol.% butanol; (h) 3rd sample purified with 100 % butanol.

As far as the TGA tests are concerned, one can observe the weight loss graphics of the first sample in Figure 33. The weight loss, due to the heating of the sample before washing, is 98.32 % corresponding to the total amount of the oleic acid, and the residual mass corresponds to SnO_2 and is equal to 0.16 %. The sample after purification with ethanol contains 45.24 % of oleic acid and 53.72 % of SnO_2 as a residual. The TGA graphics of the other two samples are similar to the ones shown in Figure 33. In the graphics one can notice the differences in the mass change under 200 ºC. The sample purified with ethanol after the addition of the oleic acid contains some alcohol, as the sample was not dried afterwards and it was used in form of a wet solid for TGA measurements. The sample that was not purified can also contain some alcohol from the previous purification. Therefore oleic acid reacts with ethanol forming esters and esters in their turn interact with alcohol via hydrogen bonds. Both hydrogen bonds and the formation of the esters affect the onset temperature, increasing it. Therefore the higher onset temperature in the first graphic can be explained by the formation of bigger amount of the ester that slows down the decomposition.
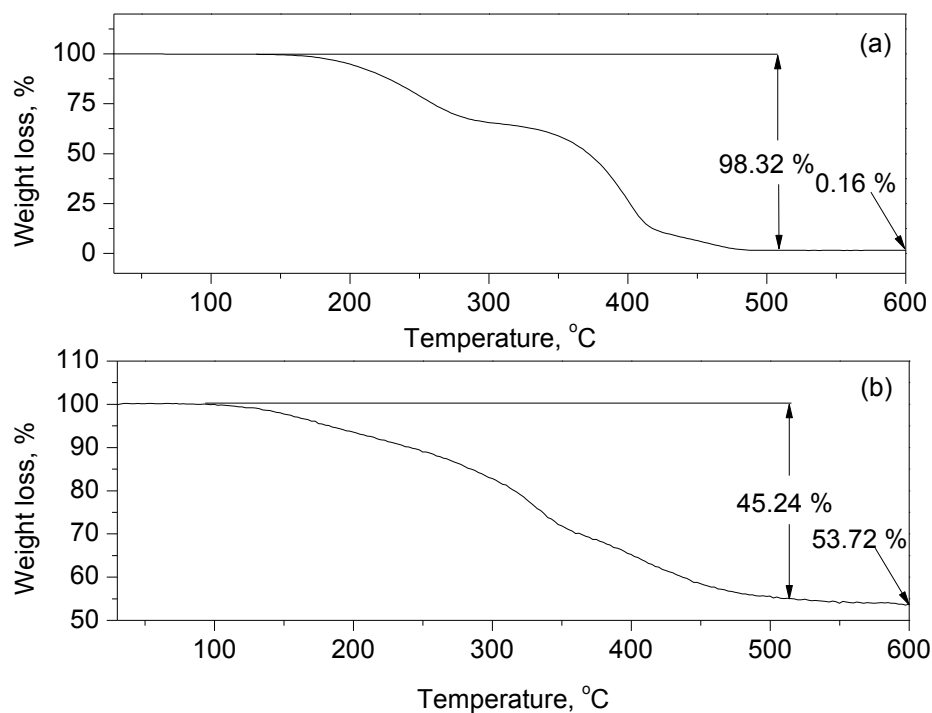
Figure 33: TGA weight loss graphics (%): (a) 1st sample after the exchange reaction with oleic acid; (b) 1st sample purified with ethanol.

In Table 2 one can find all the data regarding the size distribution of the obtained particles and molar ratio of the oleic acid with respect to tin. All three samples show a slight increase in size after the purification. It can be explained with the fact that excessive quantities of the oleic acid, i.e. some part of the signal comes from the oleic acid molecules. Although when the particles are properly washed, the signal comes only from tin nanoparticles. From the TGA weight loss graphics, one can determine the total quantities of each compound in the sample. From knowing the weight loss of each component, which in this case is only oleic acid, Sn and very small amount of alcohol one can calculate the total amount of each component. The best purified nanoparticles appear to be the ones purified with the mixtures: 80 vol.% ethanol 20 vol.% n-butanol and 50 vol.% ethanol 50 vol.% n-butanol. The results are not very precise as the investigations are performed on three samples, obtained from different syntheses. The synthesis procedure still needs some optimization in

order to obtain the same amount of the particles after each synthesis and the addition of the same quantity of the oleic acid during the purification step should be performed more precisely.

Table 2: Particles' size and molar ratio of Sn with respect to oleic acid before and after purification

Sample	Number of the Figure 33	Purification	Weight loss, %	Residual mass, %	Particles' size distribution	Molar ratio oleic acid : Sn
	(a)	None	98.32	0.16	7.1 ±0.2 nm	36.5 : 1
1	(b)	100 %ethanol	45.97	53.72	10.3 ±0.3 nm	1 : 3.0
	(c)	None	91.01	6.02	10.1 ±0.4 nm	7.9 : 1
2	(d)	80 % ethanol 20 % n-butanol	12.74	86.71	12.5 ± 0.4 nm	1 : 15.2
	(e)	50 % ethanol 50 % n-butanol	7.63	90.11	12.3 ± 0.4 nm	1 : 20.5
	(f)	None	81.84	13.89	10.1 ± 0.4 nm	3.3 : 1
3	(g)	20 % ethanol 80 % n-butanol	19.01	74.94	13.6 ± 0.4 nm	1 : 8.2
	(h)	100 % n-butanol	12.91	85.78	13.4 ± 0.4 nm	1 : 12.8

The obtained Sn nanoparticles still contained large quantities of the oleic acid. As the samples are investigated with SEM nothing but the organic layer could be seen in the sample. Tin nanoparticles are synthesized again and in Figure 34 one can observe the DLS and XRD tests. The numeric particles size distribution shows the presence of the particles

19.8 ± 0.4 nm in diameter. The XRD pattern shows the presence of the Sn tetragonal phase with strong and definite reflexes.
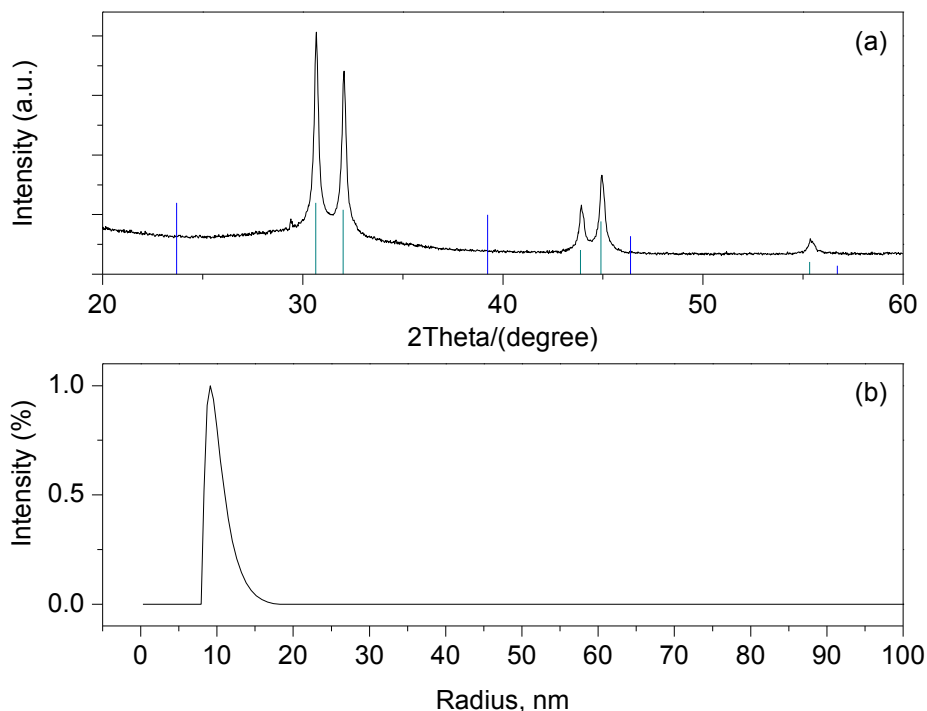

Figure 34: XRD pattern (a) and DLS measurement (b) of tin nanoparticles capped with oleic acid (References: α-Sn 00-005-0390 – blue, β-Sn 00-004-0673 – green).

The sample is divided into four parts and purified the same way, as it was described above excluding the 100 % ethanol solution, because it proved to be much more inefficient with respect to the other solutions. The sample is also washed three times instead of one in order to remove the excessive oleic acid. After the third wash the nanoparticles were more difficult to re-disperse so they had to be put in the ultrasonic bath for 1 hour with a few mL of toluene. SEM images in Figure 35 illustrate the purified tin nanoparticles obtained with 10 µm resolution.
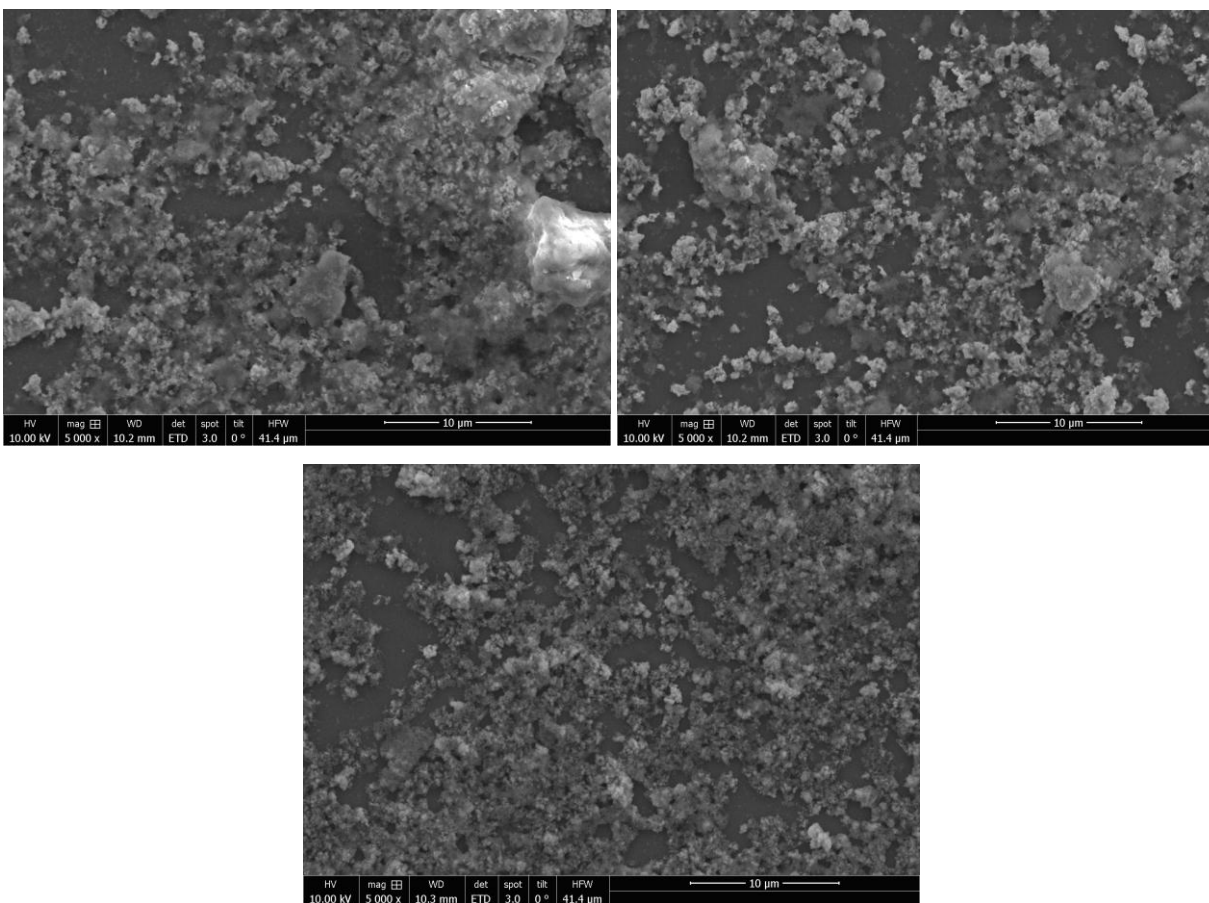
Figure 35: SEM images of the obtained tin nanoparticles purified with mixture of 80 % ethanol and 20 % n-butanol (left); 50 % ethanol and 50 % n-butanol (right); with 100 % n-butanol (below).

SEM images in Figure 36 with higher resolution show the close up of the obtained nanoparticles. All four samples appear in the form of nanoparticles embedded into an organic matrix. The samples washed with 80 % ethanol/20 % butanol and 50 % ethanol/50 % butanol seem to have more definite shape and stronger signal, which could point on the lower content of the oleic acid in the sample. This data correlates with the ones obtained before via TGA measurements.
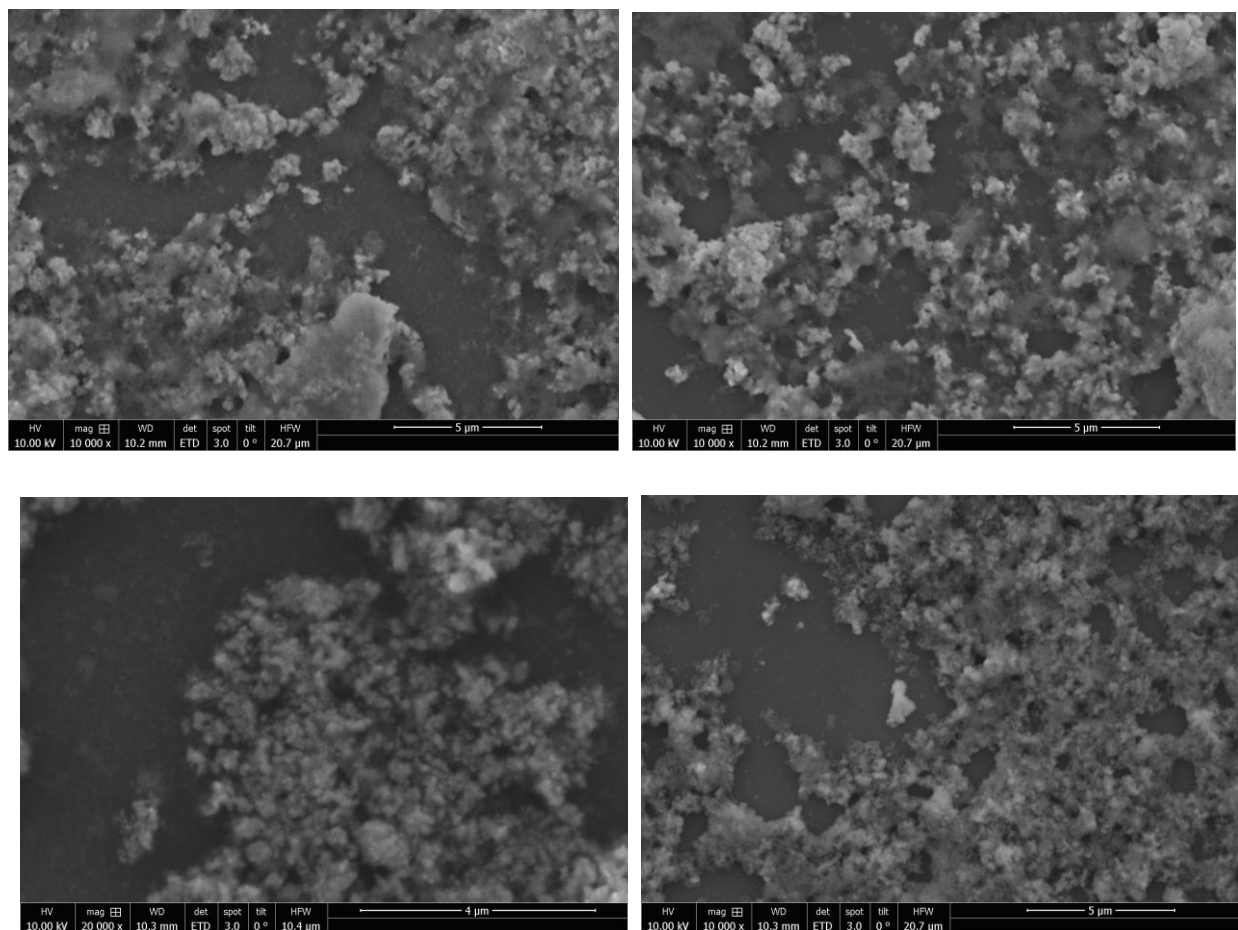
Figure 36: SEM images with higher resolution of the obtained tin nanoparticles purified with mixture of: 80 % ethanol and 20 % n-butanol (above left); 50 % ethanol and 50 % n-butanol (above right); 20 % ethanol and 80 % n-butanol (below left); 100 % n-butanol (below right).

4. SUMMARY

This work presents the synthesis and the characterization of 1D elongated germanium nanostructures in the microwave reactor. In addition, the synthesis of tin nanoparticles with narrow size distribution in the 10 nm range via hot injection method reported by Kravchyk *et al.*[42] and the characterization of the obtained nanoparticles are described in this work.

The powder XRD and TEM investigations prove the formation of the elongated germanium nanostructures with the wide size distribution in presence of tin (II) bis(bistrimethylsilyl)amide with molar ratio between Ge and Sn 2 to 1 and 5 to1. As the molar ratio is increased crystallinity could no longer be observed. The TEM images show that the obtained crystalline structures are single crystals. The use of diphenylgermane instead of germanium (II) bis(bistrimethylsilyl)amide as a precursor also results in the formation of crystalline germanium nanostructures with wide size distribution. The use of pre-synthesized tin nanoparticles capped with PVP-HDE copolymer does not lead to the formation of crystalline nanostructures.

In the second part of the work different synthetic routes which are used to obtain tin nanoparticles are studied. Thus the nanoparticles obtained via microwave thermal decomposition appear to be about 4 nm in diameter with a size distribution of about 2 %. The tin nanoparticles synthesized via hot injection method also give good results in terms of the size and size distribution. In both cases the nanoparticles are capped with oleic acid.

Lastly, the molar ratio between tin and oleic acid are studied via TGA. The results of TGA tests still speak for the presence of the excessive quantities of the oleic acid in the sample, which makes it impossible to use for the further synthesis of germanium nanostructures.

5. EXPERIMENTAL

5.1. GENERAL METHODS AND MATERIALS

The whole synthesis and working up procedure as well as storage, were carried out under inert conditions i.e. in oxygen- and water-free nitrogen or argon atmosphere using glovebox and Schlenk line techniques. The glassware was dried either by heating under a dynamic vacuum or storage in drying cabinets and transferred into the glovebox while still hot.

5.2. LIST OF CHEMICALS

Solvents and reactants were purified and desiccated using the standard techniques and stored under nitrogen or argon atmosphere. Chemicals were mostly purchased at Sigma Aldrich and ABCR and used as received. Sn(II) and Ge(II) bis[bis(trimethylsilyl)amide] were prepared through a salt elimation reaction using the dry chlorides and lithium bis(trimethylsilyl)amide.

Table 3: Used chemicals: solvents.

Nr.	Name	Molecular formula
1	Toluene	$C_6H_5-CH_3$

2	Methanol	CH_3OH
3	Ethanol	C_2H_5OH
4	Tetrahydrofuran	C_4H_8O
5	Tetrachloroethylene	$CCl_2=CCl_2$
6	n-Butanol	C_4H_9OH
7	n-Pentane	$CH_3(CH_2)_3CH_3$

Table 4: Used chemicals: reactants and other chemicals.

Nr.	Name	Molecular formula
1	Germanium (II) bis(bistrimethylsilyl)amide	$Ge[N(SiMe_3)_2]_2$
2	Tin (II) bis(bistrimethylsilyl)amide	$Sn[N(SiMe_3)_2]_2$
3	Poly(vinylpyrrolidinonehexadecene) copolymer (Antaron V-216)	$-(CH_2-CH(NC_4H_6O))-(CH_2-CH(C_{14}H_{29}))-$
4	Lithium bistrimethylsilylamide	$LiN(SiMe_3)_2$
5	Dodecylamine	$CH_3(CH_2)_{10}CH_2NH_2$
6	Oleylamine	$NH_2CH_2(CH_2)_7CH=CH(CH_2)_7CH_3$
7	Oleic acid	$CH_3(CH_2)_7CH=CH(CH_2)_7COOH$
8	1-Dodecanethiol	$CH_3(CH_2)_{10}CH_2SH$

9	Diphenylgermane	$(C_6H_5)_2GeH_2$
10	Diphenylether	$(C_6H_5)_2O$
11	1-Octadecene	$CH_2=CH(CH_2)_{15}CH_3$
12	Borane tert-butylamine complex	$(CH_3)_3CNH_2 : BH_3$
13	Tin (II) chloride	$SnCl_2$
14	Tetrabutylammonium borohydride	$[(CH_3CH_2CH_2CH_2)_4N]^+[BH_4]^-$

5.3. ANALYTICAL TECHNIQUES

5.3.1. DYNAMIC LIGHT SCATTERING (DLS)

Dynamic light scattering tests were performed using the ALV/ CGS-3 Compact Goniometer System and ALV/LSE-5004 Light Scattering Electronics and a Multiple Tau Digital Correlator. The laser wavelength used was 632.8 nm. All measurements were carried out at 296.14 K at detector position equal to 90°. The data were processed with the ALV/Static & Dynamic FIT and PLOT Program.

5.3.2.   POWDER X-RAY DIFFRACTION (XRD)

Powder X-ray diffraction experiments were performed at room temperature on a Philips X'Pert with generator Philips PW 3040/60 (mppc) and goniometer Philips PW 3050/60 (XP-2). An X-ray tube with a copper anode, current of 40 mA and tension of 40 mV emitted $Cu_{K\alpha}$ radiation (λ = 0.15418 nm) was used. The program used to record data was XPERT-PRO and to analyze data was X*Pert HighScorePlus program.

5.3.3.   SCANNING ELECTRON MICROSCOPY (SEM)

Obtained nanostructures were analyzed using a FEI Inspect F50 scanning electron microscope operated at 10 kV. A SE (secondary electron) detector was used to collect data.

5.3.4.   TRANSMISSION ELECTRON MICROSCOPY (TEM)

Structure imaging and crystallographic analyses were performed on a FEI TECNAI F20 transmission electron microscope operated at 200 kV and equipped with high angle annular dark field (HAADF) STEM and EDX detector. Digital Micrograph software was used to record and treat the images.

5.3.5. THERMOGRAVIMETRIC ANALYSIS (TGA)

Thermogravimetric analyses were performed on a Netzsch Iris TG 209 C with a 414 TASC controller in Al_2O_3 crucibles using a heating rate of 5 K/min in synthetic air atmosphere. Data processing was achieved using Proteus Analysis software.

5.4. MICROWAVE-ASSISTED GERMANIUM NANOSTRUCTURES SYNTHESIS

5.4.1 THERMAL DECOMPOSITION OF GE (II) BIS(BISTRIMETHYLSILYL)AMIDE

The germanium nanostructure synthesis was performed in a microwave reactor. The microwave reactor Monowave 300 developed by Anton Paar GmbH is shown in Figure 37. Maximum power delivered by a magnetron is 850 W, the maximum operating temperature is 300 ºC and the maximum pressure control is 30 bar. The 10 mL glass vials are usually closed with a PTFE-coated silicone septum and a PEEK (polyether ether ketone) cap prior to the synthesis procedure.

For the microwave-assisted synthesis of germanium nanoparticles germanium, bis(bistrimethylsilyl)amide was used as a precursor for thermal decomposition. In the glovebox 50 mg (0.127 mmol) of $Ge[N(SiMe_3)_2]_2$ are loaded into a 10 mL glass microwave reaction vial together with 3 mL (13.5 mmol) of dry dodecylamine, which is used as a solvent and a capping agent. The reaction vial is then sealed with a pressure cap with septum, taken out of the glovebox and then placed into the microwave reactor. The typical

synthesis program consists of three steps: heating, holding and cooling. In the first experiment the reaction mixture is heated to 240 ^{o}C, then held at 240 ^{o}C for 5 minutes and then cooled down to 55 ^{o}C. During the whole reaction the mixture is stirred at 500 rpm.

Figure 37: Monowave 300 microwave synthesis reactor.

As the reaction vial is taken out the solution is turned dark brown. In order to purify the nanoparticles 7 mL dry and degassed methanol are added and the product is centrifuged at 7500 rpm for 20 minutes. The precipitated particles are separated from the liquid and stored in a glovebox. The whole purification procedure is carried out under the argon atmosphere.

The experiment is repeated at different temperatures and reaction times in order to influence the growth process. Further reactions are carried out at 220 ^{o}C for 10 and 30 minutes, at 200 ^{o}C for 30 minutes and at 240 ^{o}C for 10 minutes. The obtained germanium nanoparticles have an acceptable size in the nanoscale range, but after the purification

process they cannot be re-dispersed in toluene, as they form bigger agglomerates that cannot be separated even after being placed in the ultrasonic bath for an hour.

5.4.2. DODECANETHIOL-CAPPED GERMANIUM NANOPARTICLES

In order to avoid the agglomeration process and to obtain stable re-dispersible Ge nanoparticles in nano range, 1-dodecanethiol is used as a stronger capping agent with respect to dodecylamine. 26 mg (0.128 mmol) of dry 1-dodecanethiol is loaded into a 10 mL glass microwave reaction vial together with 50 mg (0.127 mmol) of Ge[N(SiMe$_3$)$_2$]$_2$ and 3 mL (13.5 mmol) of dry dodecylamine in the glovebox. The reaction vial is then sealed with a pressure cap with septum, and placed into the microwave reactor. The microwave program always consists of three steps. The reaction mixture is heated to 200 ^{o}C for 30 minutes. After 30 minutes the solution becomes light orange in colour. The absence of dark brown colour shows that no nanoparticles have formed. Consequently the program is started one more time raising the temperature to 220 ^{o}C for another 30 minutes. The colour of the solution points to the assumption that the reactants still have not reacted until the end, so the temperature is raised to 240 ^{o}C and the reaction goes on for another 30 minutes. The colour of the solution turns into a dark brownish-grey, as germanium reacted with 1-dodecanethiol forming germanium thiolate.

Another option for obtaining 1-dodecanethiol-capped Ge nanoparticles is to make the surface exchange during the purification step. Ge nanoparticles are obtained following the procedure described in the section 5.4.1. The purification step begins by adding 7 mL methanol followed by the centrifugation at 7500 rpm for 20 minutes. Then the precipitated nanoparticles are separated from the liquid and a small drop (ca. 0.5 mL, 2.1 mmol) of 1-dodecanethiol is added together with 2 mL of dry toluene. The solution is placed into the ultrasonic bath for 15 minutes. 7 mL of methanol is then added to the solution, it should

appear slightly turbid followed by another centrifugation at 7500 rpm for 20 minutes. After the precipitated nanoparticles are separated from the liquid they can be easily re-dispersed in toluene. The obtained nanoparticles are stored in glovebox.

5.4.3. TIN (II) BIS(BISTRIMETHYLSILYL)AMIDE AS THE PRECURSOR FOR THE FORMATION OF TIN CATALYST SEEDS

In order to obtain crystalline structures tin nanoparticles are used as catalyst seeds in the SLS growth mechanism described in the chapter 1.1. $Sn[N(SiMe_3)_2]_2$ is used as a precursor for tin nanoparticles formation. In the glovebox 15 mg (0.0341 mmol) of $Sn[N(SiMe_3)_2]_2$ are loaded into the 10 mL glass reaction vial together with 33 mg (0.0839 mmol) of $Ge[N(SiMe_3)_2]_2$, 3 mL (13.5 mmol) of dodecylamine and 15 mg (0.00205 mmol) of dry PVP-HDE copolymer, which is used as a surface modificator for the stabilization of tin nanoparticles. The molar ratio between the precursors in this case is equal to 1 to 2.5. The reaction vial is then sealed with a pressure cap with septum, taken out of the glovebox and then placed into the ultrasonic bath for 15 minutes so that the polymer can be distributed equally in the solution. Afterwards, the vial is transferred in the microwave reactor and the reaction mixture is heated to 240 ^{o}C for 30 minutes.

The purification step is completed following the procedure described in the section 5.4.2. The obtained nanoparticles are crystalline according to the powder XRD diffractogram (see Figure 13).

The reaction is also carried out at different temperatures such as 220 ^{o}C and 200 ^{o}C. The reaction time in all reactions stays the same: 30 minutes. As a result the size of germanium nanoparticles slightly varies.

5.4.4. THERMAL DECOMPOSITION OF DIPHENYLGERMANE IN THE PRESENCE OF TIN (II) BIS(BISTRIMETHYLSILYL)AMIDE

Diphenylgermane is used as an alternative precursor for the production of germanium nanostructures. The synthesis and the purification procedure are similar to those described in section 5.4.3. 32 mg (0.140 mmol) of $(C_6H_5)_2GeH_2$ are loaded into the 10 mL reaction vessel together with 15 mg (0.0341 mmol) of $Sn[N(SiMe_3)_2]_2$, 3 mL (13.5 mmol) of dodecylamine and 15 mg (0.00205 mmol) of dry PVP-HDE copolymer. Precursors' molar ratio is equal to 4.1 to 1. Before the reaction begins the vial was placed into the ultrasonic bath for 20 minutes and the solution had become dark orange. The reaction solution is heated to 240 °C for 30 minutes. As a result the dark brown solution is obtained, which points on the formation of Ge structures. After the purification the size of the obtained structures is measured with DLS technique and the particles appear to be ca. 300 nm.

Usually $(C_6H_5)_2GeH_2$ decomposes at temperatures above 350 °C,[32,101] but the formation of germanium nanostructures using diphenylgermane took place at 240 °C. The XRD pattern of the obtained structures is shown in Figure 21.

5.4.5. SYNTHESIS OF ELONGATED GERMANIUM NANOSTRUCTURES IN THE PRESENCE OF TIN (II) BIS(BISTRIMETHYLSILYL)AMIDE

The aim of this work is to obtain elongated crystalline germanium nanostructures. In the section 5.4.4. there is a description of how crystalline nanoparticles are obtained. In order to increase the aspect ratio a different molar ratio of precursors is taken. In the glovebox 9 mg (0.0205 mmol) of $Sn[N(SiMe_3)_2]_2$ are loaded into the 10 mL glass reaction vial together with 41 mg (0.104 mmol) of $Ge[N(SiMe_3)_2]_2$, 3 mL (13.5 mmol) of dodecylamine and 15 mg

(0.00205 mmol) of dry PVP-HDE copolymer. The molar ratio between the precursors in this case is equal 1 to 5.1. The reaction vial is then sealed with a pressure cap with septum, taken out of the glovebox and then placed into the ultrasonic bath for 15 minutes. After that the vial is placed in the microwave reactor and the reaction mixture is heated to 200 ^{o}C for 30 minutes.

The purification step is completed following the procedure described in section 5.4.2. The obtained nanostructures appear to be crystalline (see Figure 13), so the molar ratio of the further experiment is increased up to 1 : 7 and 1 : 11. For the molar ration 1 : 7, 8 mg (0.0182 mmol) of Sn[N(SiMe$_3$)$_2$]$_2$ and 50 mg (0.127 mmol) of Ge[N(SiMe$_3$)$_2$]$_2$ have been used. The synthesis procedure is repeated as described above in this section. In case of the molar ration 1 to 11, 4.4 mg (0.0100 mmol) of Sn[N(SiMe$_3$)$_2$]$_2$ and 43.4 mg (0.110 mmol) of Ge[N(SiMe$_3$)$_2$]$_2$ are taken and the experiment is repeated once again. The XRD diffractogram in Figure 15 shows that both samples are amorphous.

Another option to induce the 1D growth of germanium nanostructures is to add the germanium precursor stepwise. In this experiment 23 mg (0.0585 mmol) of Ge[N(SiMe$_3$)$_2$]$_2$ are loaded to the 10 mL reaction vial followed by the addition of 8 mg (0.0182 mmol) of Sn[N(SiMe$_3$)$_2$]$_2$, 3 mL (13.5 mmol) of dodecylamine and 15 mg (0.00205 mmol) of dry PVP-HDE copolymer. The reaction vial is then sealed with a pressure cap with septum, taken out of the glovebox and then placed into the ultrasonic bath for 15 minutes. After that the vial is placed in the microwave reactor and the reaction mixture is heated to 200 ^{o}C for 30 minutes. After the first step the reaction vial is taken into the glovebox again and an additional 22 mg (0.0559 mmol) of Ge[N(SiMe$_3$)$_2$]$_2$ are put into the solution. The final molar ratio of both precursors is 1 to 6.3. The reaction vial is placed directly into the microwave and the reaction goes on for another 30 minutes at 200 ^{o}C. The purification step is performed as usual. Figure 20 shows the XRD diffractogram of the obtained solid material. There are no crystalline Ge or Sn reflexes in the diffraction pattern, which can be attributed to the amorphous nature of the product.

5.4.6. SYNTHESIS OF ELONGATED GERMANIUM NANOSTRUCTURES IN THE PRESENCE OF TIN NANOPARTICLES

Instead of the formation of tin nanoparticles in the microwave during the synthesis of germanium nanostructures, pre-synthesized Sn nanoparticles can be used. Tin nanoparticles are obtained following the procedure reported by Korgel *et al.*[41] The synthesis is described in the section 5.5.1. 0.6 mL of 39.1 mmol/L tin nanoparticles capped with PVP-HDE copolymer solution in toluene, which contains 0.02 mmol of Sn nanoparticles, is placed into the snap lid container together with 1.5 mL (6.75 mmol) of dodecylamine. The solution is heated to 110 ^{o}C for two hours in order for toluene to evaporate then the solution is loaded to the 10 mL microwave reaction vial together with 45 mg (0.11 mmol) of Ge[N(SiMe$_3$)$_2$]$_2$ and 1.5 mL (6.75 mmol) of dodecylamine. The molar ratio of Sn with respect to Ge is 1 to 4.9. It is then placed into the ultrasonic bath for 15 minutes and then into the microwave reactor and heated to 200 ^{o}C for 30 minutes. As far as purification is concerned, the sample is divided into two parts. The first part is purified using dry methanol and the second part using the dry ethanol, and the purification procedure is carried out the same way as the previous ones. The XRD diffractogram shows the amorphous structure of the sample (see Figure 24).

5.5.1. SYNTHESIS OF TIN NANOPARTICLES CAPPED WITH PVP-HDE COPOLYMER

The synthesis procedure was carried out following the instructions described in the paper by Lu *et al.*[41] 2 g (0.27 mmol, mol. mass 7300 g/mol) poly (vinylpyrrolidinonehexadecene) copolymer and 18 g (105.8 mmol) diphenyl ether are degassed under vacuum at 80 ^{o}C for 30 minutes then the whole system is blanketed with argon and heated up to 180 ^{o}C. The precursor solution consists of 0.395 g (0.90 mmol) Sn[N(SiMe$_3$)$_2$]$_2$ and 0.30 g (1.8 mmol) LiN(SiMe$_3$)$_2$ in 1.45 ml (17.9 mmol) THF. The precursor solution is then quickly injected into a heated solvent and maintained at 180 ^{o}C for 30 minutes. After the reaction vessel is cooled to room temperature the Sn nanoparticles are purified.

About 18 mL of toluene is added to the Sn nanoparticles solution followed by the addition of ethanol until the solution becomes slightly turbid. The solution is then centrifuged at 8000 rpm for 10 minutes. The precipitated nanoparticles are separated from the solution and the step is repeated two more times. The purified Sn nanoparticles are redispersed in toluene and stored in the glovebox prior to use. The concentration of Sn nanoparticles in toluene is obtained via TGA measurements and is equal to 39.05 mmol/L. The XRD pattern of the obtained Sn nanoparticles is shown in Figure 25.

5.5.2. SYNTHESIS OF TIN NANOPARTICLES CAPPED WITH OLEIC ACID

The following synthesis route is carried out in accordance with the paper by Kravchyk *et al.*[42] 20 g (74.7 mmol) oleylamine are desiccated and degassed under vacuum at 140 °C for 1.5 hours. Oleylamine is then blanketed with argon and heated to 180 °C. The quick injection of the reactants is divided in three steps. First, the solution of 0.22 g (0.5 mmol) Sn[N(SiMe$_3$)$_2$]$_2$ in 1 mL octadecene is injected. Subsequently a solution of 0.60 g (3.6 mmol) LiN(SiMe$_3$)$_2$ in 2 mL THF is injected into the reaction vessel. After 10 seconds the solution of 52.2 mg (0.6 mmol) borane *tert*-butylamine complex (BTBA) in 0.6 mL THF is injected and the reaction is kept at 180 °C either for 10 seconds or for 1 hour. The reaction is terminated by putting the reaction vessel into an ice bath until cooled to room temperature. Immediately after putting the reaction vessel into the ice bath 10 mL toluene are injected into the reaction vessel.

The purification step is performed differently in different samples, although the first stage is always the same. Ethanol is added to the mixture until it appears to be slightly turbid (ca. 40 mL) and the mixture is centrifuged at 8000 rpm for 10 minutes. After the first centrifugation to the precipitated Sn nanoparticles ca. 0.1 mL (0.317 mmol) oleic acid in ca. 6 mL (58.6 mmol) tetrachloroethylene (TCE) is added. Pure ethanol, pure butanol or the mixture of both alcohols with different volume ratio is added to the solution and followed by centrifugation at 8000 rpm for 5 minutes. The step is repeated from one to five times, but ca. 1-2 mL pure toluene is used for further dispersing of Sn nanoparticles. The purified Sn nanoparticles are dispersed in toluene and stored in the glovebox prior to use. The XRD pattern of the obtained Sn nanoparticles is shown in Figure 30.

5.5.3. SYNTHESIS OF TIN NANOPARTICLES CAPPED WITH OLEYLAMINE

The synthesis is carried out following the instructions reported in the paper by Watanabe *et al.*[44] 0.68 g (3.6mmol) $SnCl_2$ are dissolved in 10 mL of very dry THF and 1.71 g (64 mmol) oleylamine (OA) which acts as a solvent and a capping agent. The solution is thoroughly mixed with 1.85 g (7.2 mmol) tetrabutylammonium borohydride (TBABH) dissolved in 10mL THF. The mixture is stirred for three hours at 30 °C under argon atmosphere and then aged statically at 12 °C for three days. The product is then collected by centrifugation at 3000 rpm for 20 minutes and washed with a n-butanol and ethanol mixture. The precipitated tin nanoparticles are then dried under vacuum and stored in a glovebox prior to use.

5.5.4. MICROWAVE-ASSISTED SYNTHESIS OF TIN NANOPARTICLES CAPPED WITH OLEIC ACID

In the glovebox 10 mg (0.02 mmol) of $Sn[N(SiMe_3)_2]_2$ are loaded into the 10 mL glass reaction vial together with 3 mL (13.5 mmol) of dodecylamine. The reaction vial is then sealed with a pressure cap with septum and placed into the microwave reactor and the reaction mixture is heated to 200 °C for 10 minutes. The colour of the solution is not changed, so the temperature is increased three times by 10 °C for 10 minutes to 230 °C, and is run for another 30 minutes until the full decomposition of the precursor.

The next sample with 10 mg (0.0228 mmol) of $Sn[N(SiMe_3)_2]_2$ and 3 mL (13.5 mmol) of dodecylamine is placed into the microwave reactor and is heated to 230 °C for 30 minutes. The solution becomes dark brown and is then purified. 5 mL of ethanol are added to the

solution and it is appears slightly turbid. The solution is then centrifuged at 8000 for 10 minutes. To the precipitated Sn nanoparticles ca. 0.05 mL (0.168 mmol) oleic acid in ca. 2 mL (19.5 mmol) TCE and ca. 5 mL of ethanol are added. The solution is placed in the ultrasonic bath for 15 minutes followed by centrifugation at 8000 rpm for 10 minutes. The Sn nanoparticles are then washed 2 more times and the precipitate is stored in the glovebox. The XRD pattern of the obtained Sn nanoparticles is shown in Figure 28.

ABBREVIATIONS

1D, 2D, 3D	1-dimensional, 2-dimensional, 3-dimensional
approx.	Approximately
BSE	Back scattered electron
CVD	Chemical vapour deposition
DLS	Dynamic light scattering
EDX	Energy-dispersive x-ray (spectroscopy)
EELS	Electron energy loss spectroscopy
etc.	et cetera
FFT	Fast Fourier transformation
HDMS	hexamethyldisilazane
i.e.	id est
MBE	Molecular beam epitaxy
PEEK	polyether ether ketone
PLD	Pulsed laser deposition
PTFE	polytetrafluoroethylene
PVP-HDE	polyvynilpyrrolidone-hexadecene
SE	secondary electron
SEM	Scanning electron microscopy
SLS	solid-liquid-solid
TCE	tetrachloroethylene
TEM	Transmission electron microscopy

TGA	Thermogravimetric analysis
THF	tetrahydrofuran
WDX	Wavelength-dispersive x-ray (spectroscopy)
XRD	x-ray diffraction

LIST OF FIGURES AND TABLES

LIST OF REFERENCES

[1] Mullane, E., Kennedy, T., Geaney, H. and Ryan, K.M., *ACS Appl. Mater. Interf.,* **2014**, 18800-18807.

[2] Lee, W.-J., Sharp, J., Umana-Membreno, G.A., Dell, J. and Faraone, L., *Mater. Sci. Semicond. Process.,* **2015**, 30, 413-419.

[3] Yin, H.-B., Cai, H.-H., Cai, J.-Y., Teng, J.-W. and Yang, P.-H., *Mater. Lett.,* **2013**, 109, 108-111.

[4] Ghafarinazari, A. and Mozafari, M., *J. of Alloys and Compounds,* **2014**, 616, 442-448.

[5] Liu, Y., Jin, B., Li, D.-J., Zeng, X.-Q. and Lu, J., *Surface & Coatings Technology,* **2015**, 261, 219-226.

[6] Schubert, U., Hüsing, N., *Synthesis of inorganic materials,* (Weinheim : Wiley-VCH), **2012**.

[7] R. S. Wagner and W. C. Ellis, *Appl. Phys. Lett.,* **1964**, 4, 5, 89-90.

[8] Barth, S., *et al., Progress in Mat. Science*, **2010**, 55, 563-627.

[9] Vaughn II, D.D. and Schaak, R.E., *Chem. Soc. Rev.,* **2013**, 42, 2861-2879.

[10] Chiu, H.W. and Kauzlarich S.M., *Chem. Mater.* **2006,** 18, 1023-1028.

[11] Ma, X., Wu, F. and Kauzlarich S.M., *J. Solid State Chem.,* **2008**, 181, 1628– 1633.

[12] Taylor, B.R., Kauzlarich, S.M., Delgado G.D. and Lee, H.W.H., *Chem. Mater.,* **1999**, 11, 2493–2500.

[13] Tanke, R.S., Kauzlarich, S.M., Patten, T.E., Pettigrew, K.A., Murphy, D.L., Thompson M.E. and Lee, H.W.H., *Chem. Mater.,* **2003**, 15, 1682–1689.

[14] Henderson, E.J., Seino, M., Puzzo, D.P. and Ozin G.A., *J. Amer. Chem. Soc.,* **2010**, 7683– 7691.

[15] Dag, Ö., Henderson, E.J. and Ozin G.A., *SMALL*, **2012**, 8, 6, 921–929.

[16] Hoffman, M. and Veinot J.G.C., *Chem. Mater.,* **2012**, 24, 1283–1291.

[17] Wu H.P. et al., *Mater. Lett.,* **2006**, 60, 986–989.

[18] Prabakar, S., Shiohara,A., Hanada, S., Fujioka, K., Yamamoto, K. and Tilley, R.D.,*Chem. Mater.,* **2010**, 22, 482–486.

[19] Chou, N.H., Oyler, K.D., Motl, N.E. and Schaak R.E., *Chem. Mater.,* **2009**, 21, 4105–4107.

[20] X. M. Lu, B. A. Korgel and K. P. Johnston, *Chem. Mater.,* **2005**, 17, 6479–6485.

[21] D. C. Lee, J. M. Pietryga, I. Robel, D. J. Werder, R. D. Schaller and V. I. Klimov, *J. Am. Chem. Soc.,* **2009**, 131, 3436–3437.

[22] Zaitseva, N., Dai, Z.R., Grant, C.D., Harper, J. and Saw C., *Chem. Mater.,* **2007,** 19, 5174-5178.

[23] Schrick, A.C. and Weinert, C.S., *Mater. Research Bulletin,* **2013**, 48, 4390–4394.

[24] Gerung, H., Bunge, S.D., Boyle, T.G., Brinker S.J. and Han S.M., *Chem. Commun.,* **2005,** 1914–1916.

[25] O´Regan, C.,Biswas, S., Petkov, N. and Holmes, J.D., *J. Mater. Chem.,* **2004**, 2, 14-33.

[26] Zahedifar, M., Hosseinmardi, F., Eshraghi, L. and Ganjipour, B., *Radiat. Phys. Chem.,* **2011**, 324-327.

[27] Le, S.T., Jannaty, P., Zaslavsky, A., Dayeh, S.A. and Picraux, S.T., *Appl. Phys. Lett.,* **2010**, 96, 262102.

[28] Lotty, O., Biswas, S., Ghoshal, T., Glynn, C., O'Dwyer, C., Petkov, N., Morris, M.A. and Holmes, J.D., J. *Mater. Chem.,* **2013**, 4450-4456.

[29] Barth, S., Boland, J.J. and Holmes, J.D., *Nano Lett.,* **2011**, 11, 1550–1555.

[30] Lotty, O., Biswas, S., Ghoshal, T., Glynn, C., O'Dwyer, C., Petkov, N., Morris, M. and Holmes, J.D., *J. Mater. Chem.,* **2013,** 1, 4450-4456.

[31] Xiang, Y., Cao, L., Arbiol, J., Brongersma, M.L. and Morral A.F.I., *Appl. Phys. Lett.,* **2009**, 94, 163101.

[32] Chockla, A.M., Harris, J.T. and Korgel, B.A., *Chem. Mater.,* **2011**, 1964-1970.

[33] Lu, XT., Harris, J.T., Villarreal, J.E., Chockla, A.M. and Korgel, B.A., *Chem. Mater.,* **2013**, 2172-2177.

[34] Barth, S., Koleśnik, M.M., Donegan, K., Krstić, V. and Holmes, J.D., *Chem. Mater.,* **2011**, 23, 3335–3340.

[35] Thombare, S.V., Marshall, A.F. and McIntyre, P.C., *J. Appl. Phys.,* **2012**, 112, 054325.

[36] Mullane, E., Geaney, H. and Ryan K.M., *Chem. Commun.,* **2012**, 48, 5446–5448.

[37] Geaney, H., Dickinson, C., Barrett, C.A. and Ryan K.M., *Chem. Mater.,* **2011**, 23, 4838–4843.

[38] Lensch-Falk, J.L., Hemesath, E.R., Perea D.E. and Lauhon, L.J., *J. Mater. Chem.,* **2009**, 19, 849–857.

[39] Olesinski, R.W. and Abbaschian, G.J., *Bull. All. Phase Diagr.*, **1984**, 265-271.

[40] Wang, F., Tang, R., Yu, H., Gibbons, P.C. and Buhro, W.E., *Chem. Mater.* **2008,** *20,* 3656–3662.

[41] Lu, XT., Hessel, C.M., Yu, Y., Bogart, T.D. and Korgel B.A., *Chem. Eur. J.,* **2014**, 20, 5874 – 5879.

[42] Kravchyk, K., Protesescu, L., Bodnarchuk, M.I., Krumeich, F., Yarema, M., Walter, M., Guntlin, C. and Kovalenko, M.V., *J. Am. Chem. Soc.,* **2013**, 135, 4199–4202.

[43] Yang, C.-S., Liu, Q. and Kauzlarich, S.M., *Chem. Mater.,* **2000**, 12, 983-988.

[44] Watanabe, R. and Ishizaki, T., *Bull. Chem. Soc. Jpn.,* **2013**, 86, 5, 642650.

[45] Kessler, M.T., Hentschel, M.K., Heinrichs, C., Roitsch, S. and Prechtl, M.H.G., *RSC Advances,* **2014**, 14149-14156.

[46] W. X. Chen, J. Zhao, J. Y. Lee, Z. L. Liu, *Chem. Lett.,* **2004**, 33, 474.

[47] F. Liu, Y. Chang, F. Ko, and T. Chu, *Mater. Lett.*, **2004**, 58, 373.

[48] Kajbafvala, A., Zanganeh, S., Kajbafvala, E., Zargar, H. R.,Bayati, M. R. and Sadrnezhaad, S. K. *J. Alloys and Compounds.,* **2010,** 325-329.

[49] Fouad, O. A. and El-Shall, M. S., *Nano,* **2012**, 7, 5, 1250034.

[50] Wu, J., Yang, H., Li, H., Lu, Z., Yu, X. and Chen, R., *J. Alloys and Compounds.,* **2010**, 498, 2, L8-L11.

[51] H. Cheng *et al., J. of Crystal Growth,* **2007**, 299, 34–40.

[52] Galema, S.A., *Chem. Soc. Rev.,* **1997**, 26, 233-238.

[53] Perreux, L. and Loupy A., *Tetrahedron,* **2001**, 57, 9199-9223.

[54] Lewis et al., *J. Polym. Sci.,* **1992**, 1647-1653.

[55] Majetich, G. and Hicks R., *J. Microwave Power and Electromagnetic Energy,* **1995**, 30, 1, 27-45.

[56] Binner, J.G., Hassine, N.A. and Cross, T.E., *J. Mater. Chem.*, **1995**, 5389-5393.

[57] Tsuji, M., Hashimoto, M., Nishizawa, Y., Kubokawa, M. and Tsuji T., *Chem. Eur. J.,* **2005**, 11, 440 – 452.

[58] Hanrath, T. and Korgel, B.A., *J. Am. Chem. Soc.,* **2004**, 126, 15466-15472.

[59] Holmberg, V.C. and Korgel B.A., *Chem. Mater.*, **2010**, 22, 3698–3703.

[60] Yang, H.-J. and Tuan, H.-Y., *J. Mater. Chem.,* **2012**, 22, 2215–2225.

[61] Yuan, F.-W., Yang, H.-J. and Tuan, H.-Y., *Amer. Chem. Soc.,* **2012**, 9932-9942.

[62] Collins, G. and Holmes J.D., *J. Mater. Chem.,* **2011**, 21, 11052–11069.

[63] H. Adhikari, P. C. McIntyre, S. Sun, P. Pianetta and C. E. D. Chidsey, *Appl. Phys. Lett.,* **2005**, 87, 263109.

[64] Collins, G., Fleming, P., Barth, S., O'Dwyer, C., Boland, J.J., Morris, M.A. and Justin D. Holmes, J.D., Chem. Mat., **2010,** 22, 6370-6377.

[65] Holmberg, V.C., Rasch, M.R. and Korgel B.A., *Langmuir*, **2010**, 14241–14246.

[66] Fok, E., Shih, M., Meldrum, A. and Veinot, J.G.C., *Chem. Commun.,* **2004**, 386-387.

[67] Mullane, E., Kennedy, T., Geaney, H. and Ryan, K.M., *ACS Appl. Mater. Interf.,* **2014**, 18800-18807.

[68] Lee, W.-J., Sharp, J., Umana-Membreno, G.A., Dell, J. and Faraone, L., *Mater. Sci. Semicond. Process.,* **2014**, 30, 413-419.

[69] Yin, H.-B., Cai, H.-H., Cai, J.-Y., Teng, J.-W. and Yang, P.-H., *Mater. Lett.,* **2013**, 109, 108-111.

[70] Kellner R., *Analytical chemistry* (Weinheim [u.a.] : Wiley-VCH), **1998**.

[71] Krischner H., Einführung in die Röntegenfeinstrukturanalyse (Vieweg, Braunschweig /Wiesbaden), **1990**, 61-122.

[72] *in accord. with* http://www.hzdr.de/db/Cms?pOid=11644&pNid=0

[73] Sartor M., *Dynamic light scattering* (University of California San Diego).

[74] Podzimek S., Light scattering, size exclusion chromatography and asymmetric flow field flow fractionation (Hoboken, NJ : Wiley & Sons), 2011.

[75] in accord. with http://www.lsinstruments.ch/technology/dynamic_light_scattering_dls/

[76] http://www.uzaktanegitimplatformu.com/UEP/uep_ylisans/ey2/ey2_download/Practice%20Guide_Section%202_TGA.pdf

[77] http://web.abo.fi/instut/biofuelsGS-2/kursen/%C3%85/lectures/Lectrure_Thermal%20Analysis.pdf

[78] http://www.perkinelmer.com/cmsresources/images/44-74556gde_tgabeginnersguide.pdf

[79] *in accord. with* http://www.pharmatutor.org/articles/thermogravimetry

[80] *in accord. with* http://en.wikipedia.org/wiki/File:Whewellite_tga.jpg

[81] http://www.andersonmaterials.com/tga.html

[82] Amelinckx S., *Electron microscopy* (Weinheim [u.a.] : Wiley-VCH), **1997**.

[83] *in accord. with* http://www4.nau.edu/microanalysis/microprobe-sem/instrumentation.html

[84] Knoll G.F., *Radiation detection and Measurement*, (New York, NY [u.a.] : Wiley), **2000**.

[85] http://www.cobham.com/media/160745/rfa21_semedx_imaging_modes_4pg_041209.pdf

[86] Williams D.B., Carter C.B., *Transmission electron microscopy. A textbook for material science* (Springer), **2009**.

[87] http://ricordidimenticati.tumblr.com/post/33310625950/uem-and-tem-diffraction-patterns-for-amorphous

[88] Kanoun M., Busseret C., Poncet A., Souifi A., Baron T., Gautier E., *Sol.-St. El.,* **2006,** 1310-1314.

[89] Y. Kanemitsu, H. Uto, Y. Masumoto and Y.Maeda, *Appl. Phys. Lett.,* **1992,** 61, 2187.

[90] Melnikov, D.V., Chelikowsky, J.R., *Sol. St. Comm.,* **2003,** 127, 5, 361-365.

[91] Prabakar, S., Shiohara, A., Hanada, S., Fujioka, K., Yamamoto, K., Tilley, R.D., *Chem. Mat.,* **2010,** 482-486.

[92] Yin, HB., Cai H.-H.,Cai J.-Y., Teng, J.-W., Yang, PH., *Mat. Lett.,* **2013,** 109, 108-11.

[93] Dai, D.X., Piels, M., Bowers, J.E., *IEEE J. Sel. Top. Quant. El.,* **2014,** 3802214.

[94] Yang, Y., Han, G., Guo, PF., Wang, W., Gong, X., Wang, LX., Low, K.L.,Yeo, YC., *IEEE Trans. El. Dev.,* **2013,** 4048-4056.

[95] Guter, W., Schone, J., Philipps, S. P., Steiner, M., Siefer, G., Wekkeli, A., Welser, E., Oliva, E., Bett, A. W., Dimroth, F. *Appl. Phys. Lett.* **2009,** 94, 223504.

[96] Gerung H., Bunge S. D., Boyle T. J., Brinkerab C. J. and Hana S. M. *Chem. Commun.,* **2005,** 1914–1916.

[97] Singh, S., Neculaes, V.B., Lissianski V., Rizeg, G., Bulumulla, S.B., Subia, R., Manke, J., *Fuel,* **2015,** 140, 495-501.

[98] Swanson, H.E. and Tatge, E., *Natl. Bur. Stand. (U.S.), Circ.*, **1951**.

[99] Swanson, H.E. and Fuyat, R.K., *Natl. Bur. Stand. (U.S.), Circ.,* **1953**.

[100] Swanson, H.E. and Tatge, E., *Natl. Bur. Stand. (U.S.), Circ.,* **1953**.

[101] Tuan, H.-Y., Lee, D.C., Hanrath, T. and Korgel, B.A., *Chem. Mater.,* **2005**, 17, 5705-5711.